Ore Geology Reviews 139 (2021) 104559

Contents lists available at ScienceDirect

Ore Geology Reviews

journal homepage: www.elsevier.com/locate/oregeorev

Rees and other critical raw materials in Cretaceous Mediterranean-type bauxite: The case of the Sardinian ore (Italy)

Giovanni Mongelli [a], Paola Mameli [b,*], Rosa Sinisi [c], Roberto Buccione [a], Giacomo Oggiano [b]

[a] Department of Sciences, University of Basilicata, Viale dell'Ateneo Lucano 10, 85100 Potenza, Italy
[b] Department of Chemistry and Pharmacy, University of Sassari, Via Piandanna 4, 07100 Sassari, Italy
[c] Institute of Methodologies for the Environmental Analysis, National Research Council of Italy, C/da S. Loja, 85050 Tito Scalo, PZ, Italy

ARTICLE INFO

Keywords:
Critical raw materials
REEs
Mediterranean-type bauxite
Supply risk
Sardinia

ABSTRACT

Mediterranean-type bauxite deposits in Sardinia formed during the Upper Cretaceous (Cenomanian–Turonian) due to the emergence of the south European margin of the Alpine Tethys in an area affected by monsoonal climate. The deposits were controlled by the structural frame formed in a transpressive tectonic regime and unconformably overlie carbonate rocks of different age and composition, which led to the formation of different bauxite types. In general, in the Sardinian bauxite deposits, boehmite is the main Al-phase, kaolinite is the main Si-rich mineral, and hematite as well as goethite are the Fe-rich phases. Secondary authigenic anatase and detrital rutile control the Ti contents. Eu/Eu* anomalies show that the bauxite types were derived from the Variscan basement. However, there are differences in Al_2O_3 and SiO_2 contents, which suggest there was localised variability in the extent of epigenetic replacement of kaolinite by boehmite. R-mode factor analysis suggests that most critical raw materials (as defined by the devoted European Union working group), such as Sc, Ga, Nb, Hf, Ta, and W, covary with Al_2O_3 contents. In the Si-poor bauxite, these metals of economic interest are likely controlled by boehmite, whereas in the Si-rich bauxite they are mostly controlled by weathering-resistant minerals. Rare earth element (REE)-rich minerals, including fluorocarbonates and cerianite, are concentrated in the basal, illuvial horizon, especially in the silica-rich bauxite (ΣREE = 1006–2034 ppm). Cerianite formation required Ce oxidation, whereas fluorocarbonate formation involved mobilisation of trivalent REEs and further fluoride complexation. Both REE-rich mineral phases precipitated under alkaline pH conditions near to the carbonate bedrock. Our evaluation of the critical raw materials distribution in the Sardinian bauxite, coupled with the "economic importance" and "supply risk" parameters, indicate the ore contains large amounts of metals characterised by a "supply risk", such as light and heavy REEs, and metals of "economic importance", such as V and W. In this way, the Sardinian bauxite deposits could be reconsidered as a potential source of critical raw materials.

1. Introduction

An increasingly wide range of metals are utilised by society and its technological needs. In addition to the most common metallic elements (Fe, Cr, Ni, and Mn), and base (Cu, Zn, and Pb), light (Al), and precious metals, modern technology relies on nearly all the stable elements in the Periodic Table (Graedel et al., 2015). Consequently, there is growing global concern over the long-term availability of secure and adequate supplies of these metals. Critical raw materials (hereafter CRM) are those of increasing economic importance that might be susceptible to future scarcity, and are vulnerable to politically or economically driven fluctuations in their supply (Gunn, 2014; Chakhmouradian et al., 2015). For sample, in 2010, the unexpected abrupt reduction of export quotas for rare earth elements (REEs) from China revealed a vulnerability in REE supply that impacted a wide range of western high-technology industries. Several low-solubility trace elements are critical in a wide range of high technology devices, and the latest report of the European Union on critical raw materials (European Commission, 2020), included light REEs (LREEs; La–Sm), heavy REEs (HREEs; Eu–Lu), Sc, V, Co, Ga, Sr, Nb, Hf, Ta, and W, as well as bauxite, due to the importance of the latter for the production of Al. For the REEs, Eu, Tb, Y, Nd, Pr, and Dy are critical, due to their increasing use in decarbonising the energy sector

* Corresponding author.
E-mail address: mamelip@uniss.it (P. Mameli).

https://doi.org/10.1016/j.oregeorev.2021.104559
Received 8 June 2021; Received in revised form 29 October 2021; Accepted 30 October 2021
Available online 5 November 2021

and magnet production (Guyonnet et al., 2015; Jaroni et al., 2017).

Bauxite occurs in residual deposits that form in humid tropical to sub-tropical climates (e.g., Bardossy and Aleva, 1990; Bogatyrev and Zhukov, 2009; Mongelli et al., 2014, 2016; Abedini et al., 2020 and references therein). Bauxite can concentrate REEs and other CRM, such as Ga and Nb, to economic levels, although the palaeogeographic setting, protolith(s), climate, drainage, soil pH, and redox conditions can affect the CRM abundances (e.g., Mongelli et al., 2017).

However, variations in CRM abundance can occur even in deposits of the same age. These variations occur both vertically and laterally, at low scale (i.e., few metres), within apparently homogeneous deposits, as is the case for the bauxite deposits in northwestern Sardinia (Mameli et al., 2007). In this region, a horizon of Cretaceous bauxite deposits crops out over an area of 1000 km^2, and formed as a consequence of tectonic-driven emergence of the Mesozoic carbonate shelf around southern Europe. The bauxite overlies different carbonate rocks (mostly limestone and dolostone, with minor marlstone), which controlled the ore geometry and grade. There are four types of bauxite deposits (Combes et al., 1993; Mameli et al., 2007), which were all derived from alluvial material sourced by the previously weathered Variscan basement and mantle the karstified Middle Cretaceous palaeo-surface (MacLean et al., 1997; Mameli et al. 2020). In addition, each deposit type has macroscopic differences due to mineralogical and chemical fractionation involving the formation of an upper eluvial section, which is bleached and has a hard aphanitic matrix, which grades downward into an oolitic and Fe-rich illuvial horizon.

Here we present a petrographic, mineralogical, and geochemical study of REEs and other CRM in bauxite deposits in Sardinia, with a particular focus on the fractionation processes that affected the LREEs and HREEs. These new data and models identify and explain the differences in the various Sardinian bauxite deposits, and may be useful to increase the economic relevance of this resource.

2. Geological setting

The Mesozoic carbonate shelf in northwestern Sardinia is exposed over 1000 km^2 on a structural high that tilts eastward and formed during Aquitanian–Burdigalian rift to drift of the Sardinia–Corsica microplate. To the east, the carbonate shelf deposits are buried beneath a Miocene volcanic–sedimentary succession, and to the west, the deposits overlie the Variscan basement (Fig. 1). In addition to Miocene normal faults, which were responsible for the tilting, older compressional deformation, including folding and thrust and strike-slip faulting, affected the Mesozoic strata.

After restoration of the position of the Sardinia–Corsica microplate before its Miocene counter-clockwise drift, the Mesozoic carbonate shelf in northwestern Sardinia matches the Languedoc–Provençal continental shelf, which has similar sedimentary facies and palaeo-fauna (Mameli et al., 2020). The > 1000-m-thick Mesozoic carbonate succession was deposited in the Middle Triassic–Upper Cretaceous. The lower deposits are dolostone and inner shelf limestone and evaporite (i.e., German-type Triassic facies), and are overlain by at least 600 m of Jurassic limestone and dolostone that grade into a regressive, 20-m-thick, greenish marlstone deposited in brackish water facies (i.e., Purbeckian facies). This

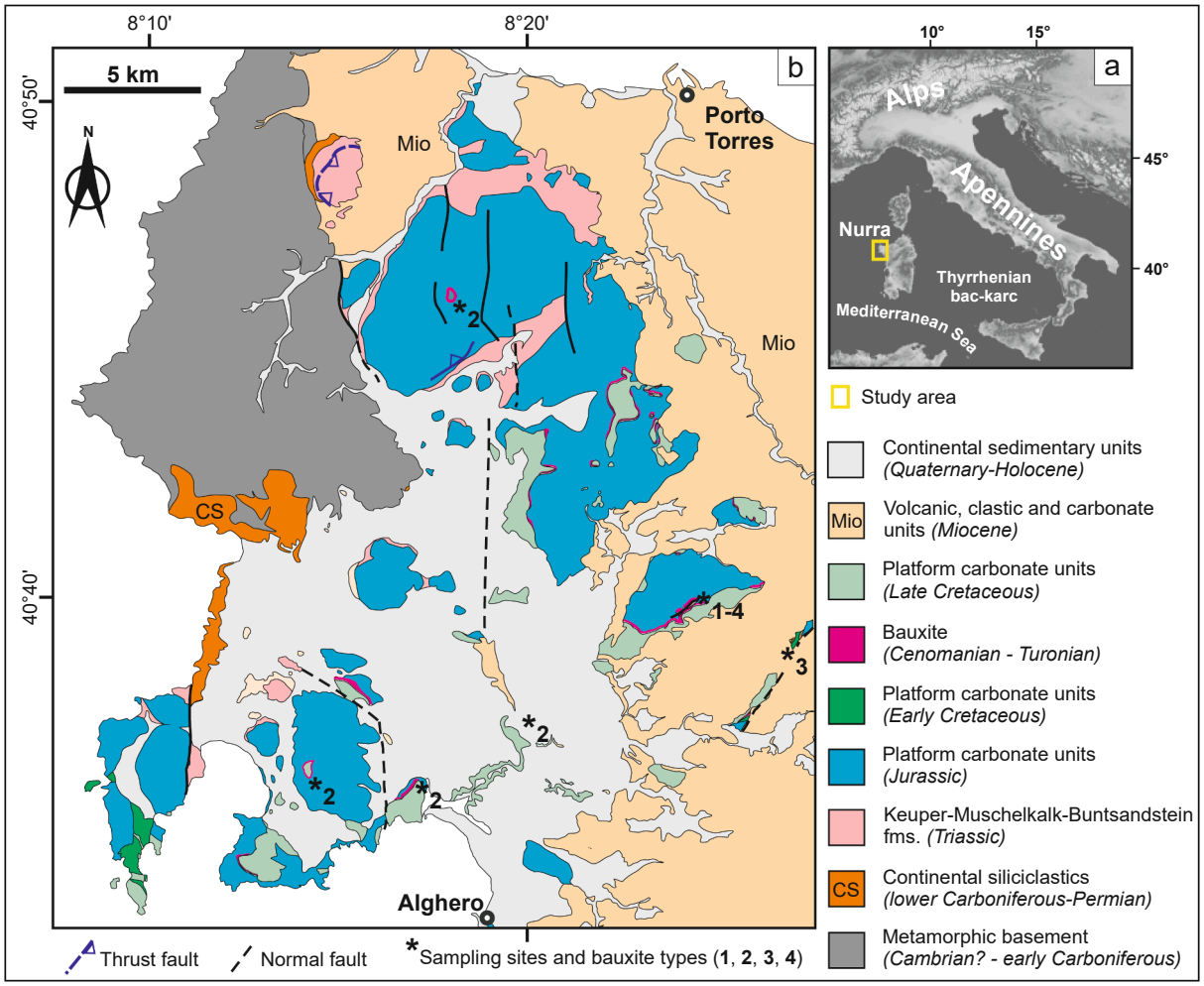

Fig. 1. Geographical map of Italy (a) and geological sketch map of northwestern Sardinia (b) showing sample locations.

marlstone is overlain by a thick (300 m), outer shelf, Lower Cretaceous bioclastic grainstone (i.e., Urgonian facies) that is Barremian–Aptian in age. A stratigraphic hiatus embracing Albian and Turonian is marked by different bauxite deposits (Combes et al., 1993; Mameli et al., 2007). The stratigraphic hiatus was caused by the emergence of the carbonate shelf over a structural high (Mameli et al., 2020), similar to the Durantian Isthmus (Blanc and Gouvernet, 1967), which was caused by the far-field effect of the transpressive motion between the Iberian and European plates (Schreiber et al., 2011).

The bauxite formed from allochthonous alluvial deposits derived from Variscan basement. These previously weathered, clayey, alluvial sediments were deposited on an exposed karstic palaeo-surface (Mameli et al., 2020). Green–grey and localised purple clay horizons occur locally beneath the bauxite deposits. The transformation into the overlying bauxite is gradational, and is reflected by lower kaolinite and increasing Al_2O_3 contents, and the appearance of an ooidal texture (Mameli et al., 2007). The bauxite overlies different lithologies, including limestone, dolostone, and, in one case, the Purbeckian marlstone.

3. Bauxite types and stratigraphy

The bauxite was sampled at different locations, including the abandoned underground mine at Olmedo. The sites were chosen to represent each deposit type based on Mameli et al. (2007). Where the profiles were entirely exposed, the upper eluvial and lower illuvial horizons were sampled.

Type 1 bauxite overlies the Purbeckian greenish marlstones and is laterally continuous, with an average thickness of 2.5–3.0 m (Fig. 2a). The upper part consists of strongly bleached, white, aphanitic, hard bauxite, which contains rare grey ooids. The eluvial horizon has a maximum thickness of 3.0 m (average = 1.5 m). The white facies grades downward into the lower illuvial horizon, which consists of oolitic, mottled bauxite that grades into clayey bauxite and clay.

In general, type 2 bauxite overlies Jurassic dolostone or dolomitic limestone. It has a regular tabular or lens-shaped geometry, but on limestone, it can have formed from type 1 bauxite that has collapsed into karst cavities. In general, the upper bleached horizon in this bauxite is a few centimetres thick and an ooid-rich, reddish to yellow deposit is dominant (Fig. 2b). This bauxite grades downward into the dolomitic footwall via a thin layer of clayey bauxite.

Type 3 bauxite overlies Barremian–Aptian limestone (i.e., Urgonian) and is poorly exposed. The maximum thickness of the lens-shaped deposits is 5 m. Reworked beds may contain limestone detritus (i.e., haramonite), which is suggestive of transport and re-deposition of an already mature bauxite.

Type 4 bauxite overlies slightly dolomitic limestone of Barremian age. This bauxite type was sampled in the Olmedo mine along a 2.5-m-thick profile (Fig. 2c). The eluvial horizon (average thickness = 1 m) is strongly bleached similar to that in the type 1 deposits. The illuvial part is yellow in colour, 1.5 m thick, and has an oolitic texture. The transition to the calcareous footwall is abrupt and marked by a < 5-cm-thick layer of clayey bauxite.

4. Materials and methods

We collected 38 samples of bauxite, including 10 of type 1, 13 of type 2, and 15 of type 4. Type 3 bauxite was not sampled due to its rarity and extensive reworking. The samples were first dried and then manually ground in an agate mortar to a very fine powder suitable for geochemical and mineralogical analysis. Whole-rock mineralogy was determined by X-ray diffraction (XRD) analysis. XRD analysis was undertaken at the Department of Chemistry and Pharmacy, University of Sassari, Italy, on randomly oriented whole-rock powders using a Bruker D2 PHASER powder X-ray diffractometer (Cu-Kα radiation, 30 kV, and 10 mA) at 2θ angles of 6°–70° and a step size of 0.02°. Mineral phases were identified from the XRD patterns using the ICDD PDF-2 database and the Bruker DIFFRAC plus EVA 14.2 software package.

Micro-morphological and *in situ* geochemical analyses were undertaken by scanning electron microscopy (SEM) using an EVO LS10 Zeiss LaB6 ESEM instrument equipped with an Oxford INCA energy dispersive X-ray spectrometer (EDS) system at the Microscopy Laboratory of the Department of Chemistry and Pharmacy, University of Sassari, Italy. Prior to the SEM observations, representative bauxite samples were polished and carbon-coated with an Edwards S-150A coating system.

Major and trace element concentrations were measured by inductively coupled plasma optical emission spectrometry (ICP-OES) and inductively coupled plasma mass spectrometry (ICP-MS), respectively, at Activation Laboratories, Ancaster, Canada. The powdered samples were dissolved by fusion with lithium metaborate/tetraborate, and the resulting molten bead was rapidly digested in a weak nitric acid solution or a multi-acid solution (for Cu, Zn, and Ni). GXR-1, NIST 694, DNC-1, GXR-4, SDC-1, GXR-6, LKSD-3, TDB-1, NOD-P-1, W-2a, DTS-2b, SY-4, CTA-AC-1, BIR-1a, NCS DC86312, ZW-C, NCS DC70009 (GBW07241), OREAS 100a (fusion), OREAS 101a (fusion), OREAS 134a (fusion), and JR-1 standards were used to calibrate the analyses. The analytical uncertainties were <±5%, except for elements with concentrations of ≤ 10 ppm, which had uncertainties of 5%–10%. Loss-on-ignition (LOI) values were gravimetrically determined after heating overnight at 950°C.

5. Results

5.1. Mineralogy and texture

XRD patterns show that all the samples consist mostly of boehmite, kaolinite, Fe oxyhydroxides, and Ti oxides (Table 1). The minerals

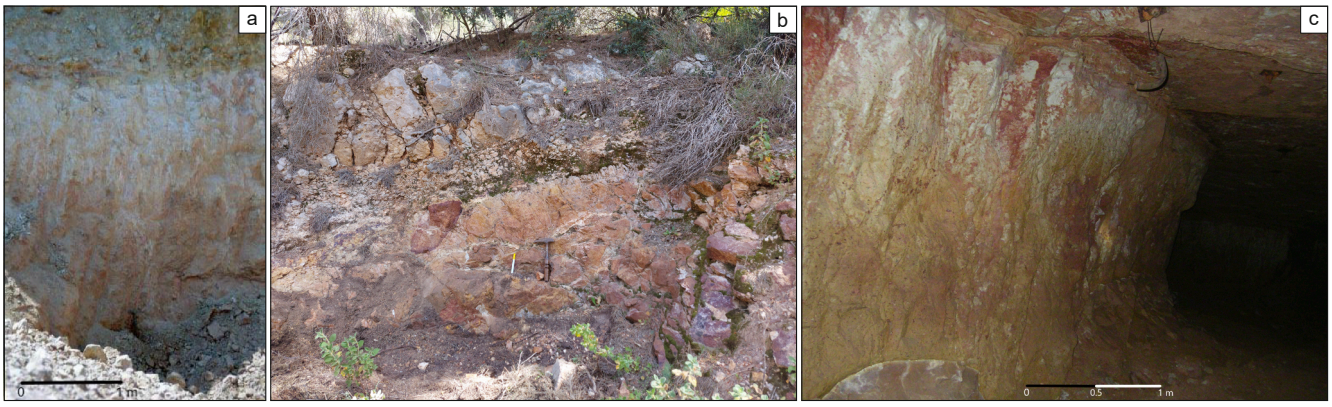

Fig. 2. (a) Type 1 bauxite in an exploration trench. (b) Type 2 bauxite in a road cut. (c) Type 4 bauxite in the underground mine at Olmedo.

Table 1
XRD mineral composition of Sardinian bauxite samples with semiquantitative interpretation. Ant: Anatase; Bhm: Boehmite; Cal: Calcite; Dsp: Diaspore; Gbs: Gibbsite; Gt: Goethite; Hem: Hematite; Ill: Illite; Kln: Kaolinite; Nalu: Natroalunite; Qtz: Quartz; Rt: Rutile; tr: trace; x: low abundance; xx: moderate abundance; xxx: high abundance.

Deposit	Sample	Bhm	Dsp	Gbs	Kln	Ill	Gt	Hem	Ant	Rt	Cal	Qz	Nalu
Type 1	T1-01	xxx	x		x		x	tr	x	x	tr		
	T1-02	xxx			xx		x	tr	x	x			
	T1-03	xxx			xx		x		x	x			
	T1-04	xxx			x		xx	x	x	tr	x		
	T1-05	xxx			xx		x	x	x	x			
	T1-06	xxx			x		x	x	x	tr	x		
	T1-07	xxx			tr		x	x	x	x			
	T1-08	xxx			x		x	x	x	x	xx		
	T1-09	xxx			xx	x	x	x	x	x	xx	tr	
	T1-10	xxx			xx	x	x	x	x	x	xx	tr	
Type 2	T2-01	xxx	x		x		x	x	x	x			
	T2-02	xxx	x		x		x	x	x	x			
	T2-03	xxx	tr		x		x	tr	x	x		tr	
	T2-04	xxx			x		xx	x	x	x			x
	T2-05	xxx	x		x		x		x	x			x
	T2-06	xxx			x		x	x	x	x			
	T2-07	xxx			xx		xx	x	x	tr			
	T2-08	xxx			xx		xx	x	x	tr			
	T2-09	xxx	tr		x		x	x	x	x			
	T2-10	x	x	x	xxx	x	xx	tr	x	x	xx	tr	
	T2-11	xx	x		xxx		xx	tr	x	x			x
	T2-12	xx	x	x	xxx		xx	tr	x	x			x
	T2-13	xx	x	x	xx		xx	tr	x	x			
Type 4	T4-01	xxx			x		x	x	x	x			
	T4-02	xxx			x		x		x	x			
	T4-03	xxx			x		x	x	x	tr			
	T4-04	xxx			xx		xx	x	x	tr			
	T4-05	xxx			x		xx	x	x	tr			
	T4-06	xxx			xx		xx	x	x	x			
	T4-07	xx					xx	x	x	x			
	T4-08	xxx			xx		xx	tr	x	x			
	T4-09	x			xxx	x	xx	x	x	x			
	T4-10	xxx			x		xx	x	x	tr			
	T4-11	x			xxx	x	x	tr	x	x			
	T4-12	xx			xx		x	x	x	x			
	T4-13	xx			xx		xx	x	x	tr			
	T4-14	xx			xx	x	xx	tr	x	x			
	T4-15	xxx			xx		xx	x	x	tr			

phases are generally readily identifiable. The main minerals in the type 1 bauxite samples are boehmite, kaolinite, anatase, hematite, and goethite, with occasional calcite, illite, quartz, and detrital rutile (Fig. 3a). Kaolinite is present in some reworked bauxite at the top of the profiles and in the basal bauxitic clay developed on the Purbeckian marls, where kaolinite occurs with illite. Type 2 bauxite samples contain boehmite, kaolinite, goethite, hematite, and anatase, with minor amounts of detrital rutile and rare diaspore, gibbsite, natroalunite, calcite, illite, and quartz (Fig. 3b). The type 4 bauxite samples contain boehmite and kaolinite in variable amounts, goethite, hematite, anatase, minor detrital rutile, and rare illite (Fig. 3c).

SEM-EDS observations revealed that the eluvial bleached horizon has similar textural features in the different bauxite types. This horizon is white in colour and comprises a homogeneous aphanitic matrix with rare, grey, boehmitic and less common Fe_2O_3-coated, millimetre-sized ooliths. The light-coloured matrix is relatively homogeneous and is boehmitic in composition. The silica-bearing phase is mostly secondary kaolinite. Monazite is the main primary REE phase and the only neoformed REE phase is cerianite, which was occasionally observed as micro-spheres within goethite pseudomorphs after marcasite (Fig. 4a).

In the type 2 bauxite deposits, the bleached horizon is thinner and contains sparse ooliths set in a fine aphanitic matrix that has pale purple patches of colouration. The strong eluviation caused indirect enrichment in residual phases, including rutile, ilmenite, and zircon, with occasional monazite and rare scheelite and osmiridium.

The illuvial horizon is generally characterised by an oolitic texture with the oolite rims enriched in Fe and cores enriched in Al (Fig. 4b). In the type 1 bauxite deposits, the illuvial bauxite is red–brown in colour and mottled, and kaolinite occurs in the matrix along with sparse ferruginous ooids. In the type 2 bauxite deposits, the illuvial horizon is poorly defined as most of the profiles consist of strongly oxidised ferruginous bauxite. The texture is ooid-dominated and ochre–yellow (6/8–7.5YR) to red–brown in colour (4/4–10R). The Fe_2O_3 content can be as high as 41.88 wt% in the brown rusty patches. Close to the contacts with the dolomitic bedrock an ooidal, brown–red, ferruginous layer contains cerianite micro-spheres within micro-cracks in Fe oxyhydroxides (Fig. 4c). REE-fluorocarbonates and phosphates are common in the ochre-coloured patches, and occur either as discrete grains within ooids or as concentric rims around Al-rich ooids.

Type 4 bauxite deposits have an oolite-dominated texture, are yellow–ochre in colour (6/8–7.5YR), and contain clusters of oriented Fe oxyhydroxides, zircon, apatite, monazite, titanite, rutile, and scheelite (Fig. 4d). The aphanitic matrix contains sparse neoformed REE phases, such as bastnasite and parisite, which occur as 2–5-μm-sized flakes, aggregates, and needle-like crystals (Fig. 4e), or replace larger minerals, which were probably monazite or allanite (Fig. 4f).

5.2. Geochemistry

Table 2 lists the geochemical data for the different bauxite types. The samples have high Al_2O_3, SiO_2, and Fe_2O_3 contents and, to a lesser extent, TiO_2 contents. Some type 1 samples (T1-8, T1-9, and T1-10) have

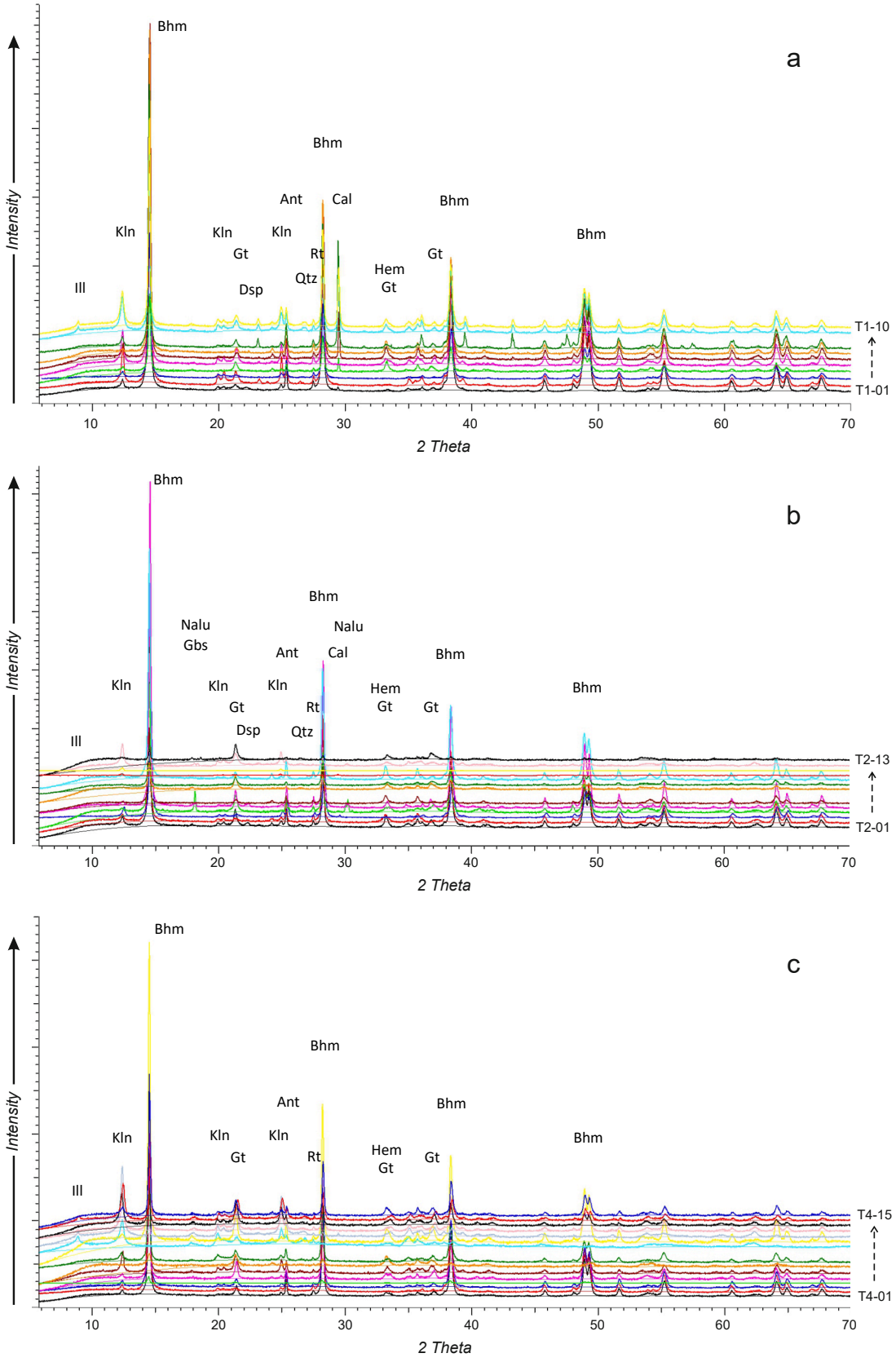

Fig. 3. XRD patterns of Type 1 (a), Type 2 (b) and Type 4 (c) bauxite samples. Mineral abbreviations are as in Table 1.

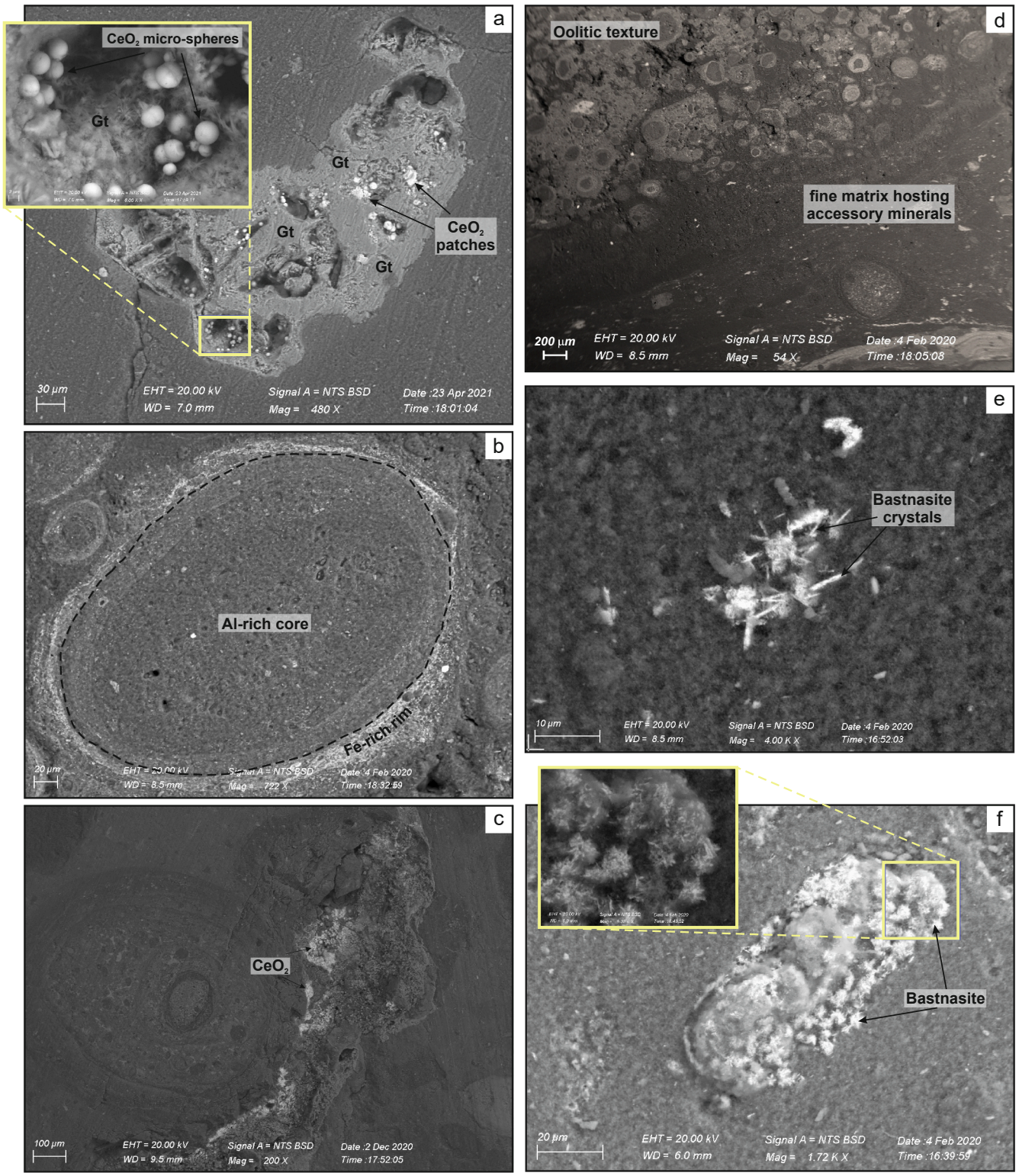

Fig. 4. BSE images of representative samples of the studied bauxites. (a) Goethite (Gt) aggregates after marcasite associated with patches and micro-spheres of cerianite (CeO_2). (b) A boehmitic oolith rimmed by Fe-bearing phases. (c) Cerianite micro-spheres in micro-cracks enriched of Fe-bearing phases. Type 2 bauxite. (d) Oolitic texture of type 4 bauxite (illuvial horizon). Microclastic swarm of accessory minerals is between ooliths. (e) Needle-like crystals of bastnasite in the type 4 bauxite (illuvial horizon). (f) Spongy aggregates of bastnasite pseudomorph after possible monazite.

CaO contents of 7–10 wt%. The Al_2O_3–SiO_2–Fe_2O_3 ternary diagram (Fig. 5; Bardossy, 1982) indicates that the deposits can be mainly classified as bauxite and subordinate clayey bauxite. Samples T2-13 and T4-9 are bauxitic Fe ore and bauxitic clay, respectively.

Box-and-whisker plots showing minimum, maximum, median, and first and third quartile values for the major elements (Fig. 6) highlight some differences between the bauxite types. Type 1 bauxite deposits have higher Al_2O_3 contents (median = 62.75 wt%, minimum = 43.71 wt %, and maximum = 71.60 wt%) as compared with type 2 (median = 53.65 wt%, minimum = 24.55 wt%, and maximum = 70.58 wt%) and

Table 2
Major, trace and rare earth elements contents of the analysed samples. D.L. = Detection Limit; n.d. = not detected; $(La/Yb)_{ch}=(La/La_{ch})/(Yb/Yb_{ch})$; $Eu/Eu^* = (Eu/Eu_{ch})/\sqrt{[(Sm/Sm_{ch})\times(Gd/Gd_{ch})]}$; $Ce/Ce^* = (Ce/Ce_{ch})/\sqrt{[(La/La_{ch})\times(Pr/Pr_{ch})]}$.

	Type 1 deposit										Type 2 deposit												
Sample	T1-01	T1-02	T1-03	T1-04	T1-05	T1-06	T1-07	T1-08	T1-09	T1-10	T2-01	T2-02	T2-03	T2-04	T2-05	T2-06	T2-07	T2-08	T2-09	T2-10	T2-11	T2-12	D.L.
wt%																							
SiO_2	3.91	11.53	8.76	2.51	8.60	2.85	1.20	3.84	10.42	16.30	6.61	5.36	7.33	3.46	2.89	2.33	9.47	6.54	3.31	32.09	28.33	21.87	0.01
Al_2O_3	71.60	63.83	66.56	53.13	61.67	67.58	67.16	58.17	54.43	43.71	61.24	64.42	68.17	53.65	70.58	54.54	37.30	47.44	67.15	27.00	35.72	35.48	0.01
Fe_2O_3(T)	5.14	4.09	2.72	27.10	10.44	10.24	10.34	6.90	8.51	6.59	12.27	10.84	3.00	20.78	7.29	25.47	34.77	24.36	10.61	17.24	14.99	24.11	0.01
MnO	0.008	0.007	0.005	0.016	0.008	0.009	0.010	0.008	0.013	0.010	0.021	0.015	0.009	0.013	0.008	0.019	0.016	0.009	0.014	0.049	0.005	0.009	0.001
MgO	0.09	0.15	0.20	0.06	0.13	0.06	0.07	0.11	0.21	0.52	0.10	0.08	0.33	0.12	0.08	0.06	0.39	0.30	0.09	0.42	0.26	0.17	0.01
CaO	0.14	0.08	0.12	0.77	0.08	0.98	0.62	8.77	7.14	9.40	0.10	0.13	0.20	0.28	0.07	0.08	0.41	0.41	0.11	4.51	0.26	0.18	0.01
Na_2O	0.02	0.09	0.07	0.02	0.05	0.02	0.16	0.08	0.07	0.08	0.05	0.02	0.02	0.31	0.08	0.02	0.07	0.04	0.04	0.14	0.29	0.16	0.01
K_2O	n.d.	0.11	0.05	0.02	0.08	0.03	0.02	0.09	0.28	0.43	0.04	0.01	0.05	0.06	0.05	0.01	0.02	0.01	0.03	0.50	0.31	0.10	0.01
TiO_2	3.126	2.879	3.562	2.685	2.841	2.740	3.490	3.397	2.295	2.261	2.831	3.281	3.816	2.972	3.040	3.360	1.388	2.141	3.176	1.517	3.392	1.874	0.001
P_2O_5	0.04	0.03	0.03	0.08	0.04	0.05	0.05	0.07	0.05	0.05	0.08	0.07	0.05	0.06	0.06	0.06	0.11	0.08	0.08	0.07	0.08	0.08	0.01
LOI	15.52	15.57	15.45	14.21	15.05	14.67	15.48	19.06	16.32	19.71	14.99	14.38	15.57	17.01	15.53	13.55	16.37	18.18	14.73	15.25	15.19	16.38	0.01
Total	99.59	98.37	97.53	100.60	98.99	99.23	98.60	100.50	99.74	99.06	98.33	98.61	98.55	98.72	99.68	99.50	100.31	99.51	99.34	98.79	98.83	100.41	
ppm																							
Sc	74	48	50	86	66	56	61	47	49	47	63	57	59	62	60	72	38	45	63	27	40	32	1
Be	6	7	12	5	9	7	7	5	6	8	6	7	15	4	4	7	11	11	8	7	5	6	1
V	611	453	479	703	697	506	603	508	407	456	707	937	960	863	555	1.226	845	848	774	442	503	708	5
Cr	710	600	520	540	580	600	680	570	460	380	500	550	530	440	390	490	350	380	540	140	180	280	20
Co	26	8	12	20	20	12	12	17	15	19	23	25	12	28	15	28	43	31	27	59	11	26	1
Ni	n.d.	n.d.	n.d.	50	50	30	n.d.	n.d.	50	100	70	50	240	60	50	110	230	230	80	265	182	190	20
Zn	n.d.	n.d.	n.d.	n.d.	n.d.	n.d.	n.d.	n.d.	n.d.	40	n.d.	n.d.	n.d.	n.d.	n.d.	n.d.	n.d.	n.d.	40	77	n.d.	n.d.	30
Ga	89	74	36	71	73	78	79	64	59	50	70	76	102	68	81	72	49	68	79	29	49	38	1
As	41	21	6	44	22	22	28	22	25	15	35	64	16	87	20	92	43	39	32	93	32	51	5
Rb	n.d.	3	3	n.d.	3	n.d.	n.d.	4	12	19	n.d.	n.d.	n.d.	n.d.	n.d.	n.d.	n.d.	n.d.	n.d.	37	13	2	1
Sr	23	18	33	63	47	65	46	43	81	122	72	37	27	145	184	39	22	17	56	33	158	54	2
Y	50.3	50.1	72	54	63.1	47.4	62.7	63	42	71	66.2	69.7	84	60.3	54	72	142	120	83.1	99	95	63	0.5
Zr	789	734	873	703	723	608	877	840	569	584	727	808	901	762	607	860	370	500	786	456	775	441	1
Nb	71.1	66.7	74	64	63.4	59.9	76.6	72.9	49.2	45	63.9	77.7	92	70.8	71.5	76	37	51	75.8	35	77	47	0.2
Mo	22	24	16	21	19	15	17	14	13	11	20	26	15	29	17	38	27	23	24	21	38	32	2
Ag	3.7	3.3	n.d.	1.9	3.4	2.8	3.9	4	2.6	1.5	3.5	3.7	2.5	3.6	2.7	2.5	1	1.3	4	0.8	1.2	1.2	0.5
In	0.6	0.4	0.6	0.4	0.5	0.5	0.6	0.5	0.4	0.3	0.4	0.5	0.4	0.4	0.3	0.4	0.2	0.3	0.4	n.d.	n.d.	0.2	0.1
Sn	14	12	15	12	14	13	17	16	10	9	13	16	12	13	14	15	7	10	16	6	13	8	1
Sb	2.9	1.5	1.4	3.7	2.6	2.1	3.2	2.6	2	2.5	5.2	12.8	3.5	8.2	2.2	11.8	4.4	6.2	6	1.1	0.7	7.5	0.2
Ba	9	14	10	23	22	15	15	17	43	41	15	15	13	21	24	17	36	13	12	66	49	29	2
Hf	21.6	19.5	22.4	19.9	19.5	15.7	24.2	22.0	14.6	15.4	19.7	22.0	26.0	20.9	16.3	25.7	10.7	14.5	21.3	12.3	20.3	12.7	0.1
Ta	3.87	4.53	4.20	4.90	4.20	3.62	3.96	3.97	3.46	3.40	4.01	4.43	5.90	4.44	3.94	4.00	2.80	3.30	4.33	2.80	6.40	4.00	0.05
W	7.6	7.2	10.0	6.0	6.8	6.9	8.1	7.4	5.9	4.0	7.4	8.6	9.0	8.8	7.4	9.0	5.0	8.0	8.4	3.0	8.0	4.0	0.1
Pb	23	17	n.d.	40	51	45	62	42	48	47	76	170	52	75	64	126	51	65	131	30	49	34	5
Bi	2.5	1.0	1.1	3.6	2.2	1.8	3.1	2.1	1.7	1.2	1.8	2.8	2.7	1.5	1.2	2.1	2.3	1.3	2.1	4.0	6.6	1.5	0.1
Th	76.80	47.00	65.00	49.60	57.80	56.00	75.70	54.70	47.40	43.30	57.20	63.00	61.00	52.80	45.80	55.00	33.40	36.80	64.40	23.00	33.50	31.80	0.05
U	14.00	13.40	15.10	14.70	13.40	12.20	16.00	9.69	11.30	10.40	13.60	13.30	24.10	14.80	12.10	18.20	20.60	14.50	15.10	10.10	19.00	17.70	0.01
La	10.30	8.24	28.30	20.00	29.50	37.50	21.40	18.50	34.90	76.60	84.20	62.20	64.00	45.50	74.70	65.40	146.00	77.10	116.00	227.00	136.00	87.70	0.05
Ce	38.20	25.50	106.00	103.00	108.00	133.00	74.30	51.20	243.00	213.00	144.00	91.60	110.00	96.60	150.00	181.00	281.00	153.00	347.00	185.00	228.00	187.00	0.05
Pr	2.50	2.05	8.48	5.57	8.04	6.68	5.22	4.64	7.16	20.50	13.70	9.42	11.70	7.93	10.40	12.60	32.70	18.80	24.90	58.60	19.50	16.60	0.01
Nd	10.10	8.68	32.30	21.90	32.90	24.40	20.60	19.30	26.40	76.20	45.60	33.20	39.40	30.80	34.70	42.20	124.00	70.70	92.00	210.00	68.70	61.40	0.05
Sm	3.25	3.07	8.40	6.50	9.11	6.27	5.98	5.96	6.90	16.90	9.10	7.62	8.80	7.40	7.70	10.30	22.40	14.80	20.60	35.00	11.90	11.00	0.01
Eu	0.893	0.889	1.900	1.640	2.080	1.450	1.440	1.420	1.420	3.450	2.000	1.820	2.130	1.650	1.660	2.350	4.900	3.440	4.250	7.470	2.560	2.260	0.005
Gd	4.72	4.64	8.50	7.50	8.89	6.01	6.85	7.16	6.04	13.90	8.09	8.26	10.40	7.84	6.65	10.40	22.20	15.40	15.60	31.20	11.00	10.30	0.01
Tb	1.20	1.19	1.90	1.70	1.99	1.44	1.63	1.70	1.37	2.30	1.81	1.99	2.30	1.70	1.62	2.20	3.20	2.70	3.08	4.10	1.90	1.50	0.01
Dy	8.85	8.74	13.00	11.00	13.00	9.55	11.80	11.70	9.05	14.00	11.90	13.40	15.90	11.20	11.40	15.70	19.20	17.70	17.80	20.60	12.30	9.90	0.01
Ho	1.77	1.81	2.70	2.30	2.55	1.88	2.38	2.42	1.74	2.90	2.35	2.59	3.50	2.19	2.21	3.30	4.00	3.80	3.21	3.70	2.60	2.00	0.01

(*continued on next page*)

Table 2 (*continued*)

	Type 1 deposit										Type 2 deposit												
Sample	T1-01	T1-02	T1-03	T1-04	T1-05	T1-06	T1-07	T1-08	T1-09	T1-10	T2-01	T2-02	T2-03	T2-04	T2-05	T2-06	T2-07	T2-08	T2-09	T2-10	T2-11	T2-12	D.L.
Er	5.48	5.51	8.60	7.30	7.77	6.09	7.59	7.46	5.39	8.30	7.03	8.05	11.70	6.72	7.08	10.00	11.70	11.50	9.78	10.40	8.60	6.30	0.01
Tm	0.952	0.916	1.370	1.150	1.320	1.040	1.310	1.200	0.950	1.240	1.200	1.340	1.800	1.090	1.240	1.550	1.570	1.660	1.570	1.470	1.370	0.900	0.005
Yb	6.54	6.27	9.70	7.80	9.13	7.12	8.96	8.48	6.54	8.50	8.15	9.19	12.80	7.33	8.84	11.20	9.70	11.20	10.40	9.00	9.30	5.80	0.01
Lu	1.050	1.010	1.570	1.260	1.410	1.160	1.470	1.350	1.030	1.330	1.280	1.450	2.050	1.240	1.360	1.760	1.570	1.770	1.680	1.310	1.420	0.960	0.002
ΣREE	95.81	78.52	232.72	198.62	235.69	243.59	170.93	142.49	351.89	459.12	340.41	252.13	296.48	229.19	319.56	369.96	684.14	403.57	667.87	804.85	515.15	403.62	
$(La/Yb)_{ch}$	1.06	0.89	1.97	1.73	2.18	3.56	1.61	1.47	3.61	6.09	6.98	4.57	3.38	4.19	5.71	10.22	10.17	18.14	3.95	4.65	7.54	17.04	
Ce/Ce*	1.78	1.47	1.62	2.31	1.66	1.99	1.67	1.31	3.64	1.27	1.01	0.90	0.95	1.21	1.28	1.16	0.96	0.59	1.49	0.95	1.53	0.38	
Eu/Eu*	0.68	0.70	0.67	0.70	0.69	0.70	0.67	0.64	0.65	0.67	0.69	0.68	0.66	0.64	0.69	0.63	0.65	0.67	0.67	0.68	0.70	0.67	

	Type 4 deposit															
Sample	T4-01	T4-02	T4-03	T4-04	T4-05	T4-06	T4-07	T4-08	T4-09	T4-10	T4-11	T4-12	T4-13	T4-14	T4-15	D.L.
wt%																
SiO_2	3.79	4.74	4.59	7.29	4.69	14.29	16.81	15.66	40.87	3.96	34.26	17.39	17.61	22.68	11.59	0.01
Al_2O_3	67.13	69.71	68.79	54.95	58.41	51.61	36.98	56.06	28.05	60.24	32.82	53.15	44.59	44.21	51.86	0.01
Fe_2O_3(T)	9.66	4.54	6.82	19.64	17.71	16.79	29.86	8.91	11.63	17.63	15.51	12.29	19.78	15.73	19.67	0.01
MnO	0.011	0.010	0.008	0.016	0.016	0.014	0.052	0.009	0.023	0.018	0.024	0.014	0.019	0.020	0.032	0.001
MgO	0.15	0.17	0.10	0.19	0.16	0.17	0.41	0.31	1.37	0.13	0.63	0.23	0.28	0.34	0.25	0.01
CaO	0.12	0.14	0.07	0.08	0.11	0.14	0.51	0.28	0.34	0.10	0.40	0.09	0.14	0.12	0.15	0.01
Na_2O	0.13	0.13	0.09	0.06	0.11	0.04	0.08	0.09	0.26	0.03	0.23	0.10	0.14	0.13	0.04	0.01
K_2O	0.01	0.02	0.02	0.16	0.02	0.09	0.67	0.52	3.19	0.03	1.05	0.23	0.23	0.47	0.11	0.01
TiO_2	3.464	3.391	3.004	2.390	2.469	2.435	1.694	2.627	1.372	2.385	1.488	2.416	1.821	2.101	1.901	0.001
P_2O_5	0.04	0.05	0.05	0.06	0.05	0.04	0.08	0.04	0.08	0.05	0.06	0.05	0.05	0.07	0.08	0.01
LOI	15.22	15.63	15.02	14.15	14.82	14.64	12.54	14.93	13.17	14.96	14.21	14.49	14.53	14.07	14.36	0.01
Total	99.73	98.53	98.56	98.99	98.57	100.26	99.69	99.44	100.36	99.53	100.68	100.45	99.19	99.94	100.04	
ppm																
Sc	1	70	57	63	82	89	74	50	60	30	68	45	77	69	70	1
Be	1	12	12	11	10	13	10	9	10	11	10	10	11	12	11	1
V	5	669	576	676	862	771	616	623	596	263	711	364	567	611	565	5
Cr	20	680	610	650	430	560	510	550	400	170	550	220	440	380	350	20
Co	1	20	26	14	43	29	29	49	33	17	42	32	28	35	32	1
Ni	20	100	80	80	187	150	120	190	160	150	140	210	200	210	220	20
Zn	30	n.d.	40	n.d.	n.d.	n.d.	n.d.	n.d.	n.d.	110	n.d.	70	30	40	50	30
Ga	1	79	81	77	67	70	59	47	64	36	70	36	63	57	53	1
As	5	27	23	21	34	44	34	35	15	23	35	25	25	42	25	5
Rb	1	n.d.	n.d.	n.d.	6	n.d.	3	28	25	142	n.d.	46	11	10	21	1
Sr	2	27	22	38	88	52	52	174	91	125	55	83	67	53	87	2
Y	0.5	72	64	61	121	77	84	125	85	96	109	107	75	96	89	0.5
Zr	1	853	859	714	584	571	639	412	637	342	552	349	551	420	505	1
Nb	0.2	84	77	68	49	58	57	36	59	31	54.3	34	56	42	47	0.2
Mo	2	19	22	16	13	16	18	20	13	6	16	5	11	11	9	2
Ag	0.5	2.5	2.4	1.8	0.6	1.5	1.6	1.9	2.8	0.9	2.7	0.9	1.5	1.1	1.3	0.5
In	0.1	0.5	0.4	0.4	0.3	0.4	0.3	n.d.	n.d.	n.d.	0.4	0.2	0.3	0.3	0.3	0.1
Sn	1	16	14	15	13	13	11	12	16	6	11	7	11	9	9	1
Sb	0.2	2.9	2.5	2.1	0.8	3.8	3	6.5	3	2.2	3.2	2	2.5	3	2.7	0.2
Ba	2	11	8	11	19	15	19	61	69	199	11	113	46	49	81	2
Hf	0.1	22.1	25.1	20.0	15.1	17.2	18.3	11.0	17.2	10.0	14.8	10.3	16.3	12.5	14.3	0.1
Ta	0.05	5.60	5.20	4.80	3.10	4.40	4.80	3.00	4.80	2.70	3.61	2.80	4.70	3.50	4.00	0.05
W	0.1	15.0	19.0	7.0	18.0	8.0	6.0	22.0	5.0	3.0	6.1	4.0	7.0	5.0	5.0	0.1
Pb	5	48	32	37	60	69	54	80	87	86	80	58	53	66	66	5
Bi	0.1	2.8	3.7	3.1	21.9	3.2	2.4	1.7	2.0	1.0	1.7	1.4	1.8	2.2	2.0	0.1
Th	0.05	64.80	68.50	57.40	43.20	48.50	48.00	31.20	48.00	21.70	50.00	25.50	38.60	34.30	33.90	0.05
U	0.01	13.20	14.00	10.60	11.30	12.80	13.30	10.10	10.60	7.20	10.80	8.20	10.00	10.90	9.60	0.01

(*continued on next page*)

Table 2 (*continued*)

	Type 4 deposit														
Sample	T4-01	T4-02	T4-03	T4-04	T4-05	T4-06	T4-07	T4-08	T4-09	T4-10	T4-11	T4-12	T4-13	T4-14	T4-15	D.L.
La	0.05	24.80	12.60	24.60	189.00	54.60	70.20	153.00	173.00	556.00	284.00	462.00	53.70	80.70	84.40	0.05
Ce	0.05	99.60	35.00	89.90	426.00	198.00	208.00	423.00	328.00	374.00	700.00	746.00	934.00	1280.00	1240.00	0.05
Pr	0.01	7.94	3.83	7.95	45.80	17.00	22.40	31.70	39.40	131.00	70.30	127.00	23.70	41.60	36.90	0.01
Nd	0.05	32.40	14.90	31.30	169.00	67.40	92.50	118.00	143.00	454.00	271.00	467.00	95.80	180.00	152.00	0.05
Sm	0.01	11.00	5.60	9.80	34.30	21.50	25.30	25.60	28.10	69.40	52.40	82.00	30.00	57.90	45.20	0.01
Eu	0.005	2.620	1.520	2.370	7.760	5.080	5.750	5.590	5.610	13.200	10.400	15.700	6.530	12.600	9.820	0.005
Gd	0.01	11.80	7.50	9.80	29.20	19.80	23.10	24.20	21.60	48.70	35.40	54.80	22.90	41.70	33.70	0.01
Tb	0.01	2.70	1.90	2.10	4.90	3.90	3.70	4.20	3.30	5.80	5.43	6.90	4.20	7.10	5.70	0.01
Dy	0.01	17.00	13.80	14.30	26.20	23.60	20.60	25.10	19.00	27.80	28.90	33.80	23.60	35.80	29.60	0.01
Ho	0.01	3.60	3.00	3.00	4.80	4.70	3.90	4.90	3.70	4.70	4.87	5.70	4.40	6.20	5.30	0.01
Er	0.01	11.50	9.40	9.40	14.20	14.10	11.40	14.20	10.90	13.00	13.90	15.60	13.10	17.50	15.00	0.01
Tm	0.005	1.810	1.500	1.450	2.120	2.170	1.600	2.110	1.700	1.610	2.120	2.000	1.980	2.390	2.090	0.005
Yb	0.01	12.80	10.50	10.10	14.10	15.20	10.90	13.80	11.30	10.10	14.10	13.00	13.80	16.40	14.40	0.01
Lu	0.002	2.080	1.690	1.600	2.090	2.410	1.650	2.080	1.790	1.590	2.230	1.960	2.200	2.650	2.130	0.002
ΣREE	241.65	122.74	217.67	969.47	449.46	501.00	847.48	790.40	1,710.90	1,495.05	2,033.46	1,229.91	1,782.54	1,676.24	1,005.96	
$(La/Yb)_{ch}$	1.31	0.81	1.65	9.06	2.43	4.35	7.49	10.34	37.20	13.61	24.01	2.63	3.32	3.96	13.07	
Ce/Ce^*	1.68	1.19	1.52	1.09	1.54	1.24	1.44	0.94	0.33	1.17	0.73	6.21	5.24	5.27	0.85	
Eu/Eu^*	0.68	0.70	0.72	0.73	0.73	0.71	0.67	0.68	0.67	0.72	0.69	0.74	0.76	0.75	0.70	

type 4 deposits (median = 53.15 wt%, minimum = 28.05 wt%, and maximum = 69.71 wt%). The Fe_2O_3 contents are higher in type 2 (median = 17.24 wt%, minimum = 3.00 wt%, and maximum = 41.88 wt %) and type 4 (median = 16.26 wt%, minimum = 6.82 wt%, and maximum = 29.86 wt%) deposits than in the type 1 deposits (median = 7.71 wt%, minimum = 2.72 wt%, and maximum = 27.1 wt%). Silica contents are higher in type 4 deposits (median = 14.29 wt%, minimum = 3.79 wt%, and maximum = 40.87 wt%) than type 1 (median = 6.26 wt%, minimum = 1.20 wt%, and maximum = 16.30 wt%) and type 2 (median = 6.61 wt%, minimum = 2.33 wt%, and maximum = 32.09 wt %) deposits. TiO_2 contents are similar in the three types of deposits (type 1 median = 2.86 wt%, minimum = 2.26 wt%, and maximum = 3.56 wt %; type 2 median = 2.97 wt%, minimum = 1.03 wt%, and maximum = 3.82 wt%; type 4 median = 2.39 wt%, minimum = 1.37 wt%, and maximum = 3.46 wt%), suggesting that the type has little affect on Ti contents.

LREEs (La–Sm), HREEs (Eu–Lu), Sc, V, Co, Ga, Sr, Nb, Hf, Ta, and W were identified as critical metals in the latest European Union report on critical raw materials (European Commission, 2020). Upper continental crust (UCC)-normalised elemental patterns (Fig. 7) and descriptive statistics (Figs. 8 and 9) indicate that the different bauxite types have similar patterns, with the exception of LREEs and HREEs that are enriched in type 4 deposits. The type 4 deposits have average $(La/Yb)_{ch}$ ratios that are similar to those of type 2 deposits, although the former has larger $(La/Yb)_{ch}$ variations (type 2 $(La/Yb)_{ch} = 8.19 \pm 4.82$; type 4 $(La/Yb)_{ch} = 9.02 \pm 10.02$), with the lowest values associated with eluvial horizons (T4-2 $(La/Yb)_{ch} = 0.81$). This is also the case for the type 2 (eluvial T2-3 $(La/Yb)_{ch} = 3.38$) and type 1 (T1-2 $(La/Yb)_{ch} = 0.89$) deposits, although their average $(La/Yb)_{ch}$ ratio is lower $(La/Yb)_{ch} = 2.42 \pm 1.59$). The largest average Ce anomaly characterises the type 4 bauxite deposits (type 1 $Ce/Ce^* = 1.87 \pm 0.69$; type 2 $Ce/Ce^* = 1.04 \pm 0.32$; type 4 $Ce/Ce^* = 2.03 \pm 1.88$), and the highest values are associated with the illuvial horizon (T4-12 $Ce/Ce^* = 6.21$; T4-14 $Ce/Ce^* = 5.27$). All the bauxite types have average Eu anomalies similar to UCC (type 1 $Eu/Eu^* = 0.68 \pm 0.02$; type 2 $Eu/Eu^* = 0.67 \pm 0.02$; type 4 $Eu/Eu^* = 0.71 \pm 0.03$; UCC $Eu/Eu^* = 0.66$).

In general, all the bauxite types are enriched in CRM with respect to the UCC, with the exception of mobile Sr. Based on the median values, type 4 deposits are strongly enriched in LREEs (~6.5 × UCC, median = 864.10 ppm, minimum = 71.93 ppm, and maximum = 1884.00 ppm), HREEs (~6.5 × UCC, median = 96.18 ppm, minimum = 50.81 ppm, and maximum = 149.46 ppm), and Sc (5 × UCC, median = 68 ppm, minimum = 30 ppm, and maximum = 89 ppm), whereas type 2 deposits exhibit significant V enrichment (~7 × UCC, median = 774 ppm, minimum = 442 ppm, and maximum = 1226 ppm).

Gallium, Nb, Hf, and W have higher median contents in type 1 (Ga ~ 4 × UCC, median = 72 ppm, minimum = 36 ppm, and maximum = 89 ppm; Nb ~ 5 × UCC, median = 65.35 ppm, minimum = 45 ppm, and maximum = 76.6 ppm; Hf ~ 3 × UCC, median = 19.7 ppm, minimum = 14.6 ppm, and maximum = 24.2 ppm; W ~ 3.5 × UCC, median = 7.05 ppm, minimum = 4 ppm, and maximum = 10 ppm) and type 2 deposits (Ga 4 × UCC, median = 68 ppm, minimum = 29 ppm, and maximum = 102 ppm; Nb ~ 6 × UCC, median = 70.8 ppm, minimum = 25 ppm, and maximum = 92 ppm; Hf ~ 3 × UCC, median = 19.7 ppm, minimum = 6.2 ppm, and maximum = 26 ppm; W 4 × UCC, median = 8 ppm, minimum = 2 ppm, and maximum = 9 ppm). Tantalum has similar contents in the three types of deposits (4 × UCC). Cobalt is depleted in type 1 deposits (~0.9 × UCC), and displays minor enrichment with respect to the UCC in the type 2 (~1.6 × UCC) and type 4 (~1.9 × UCC) deposits.

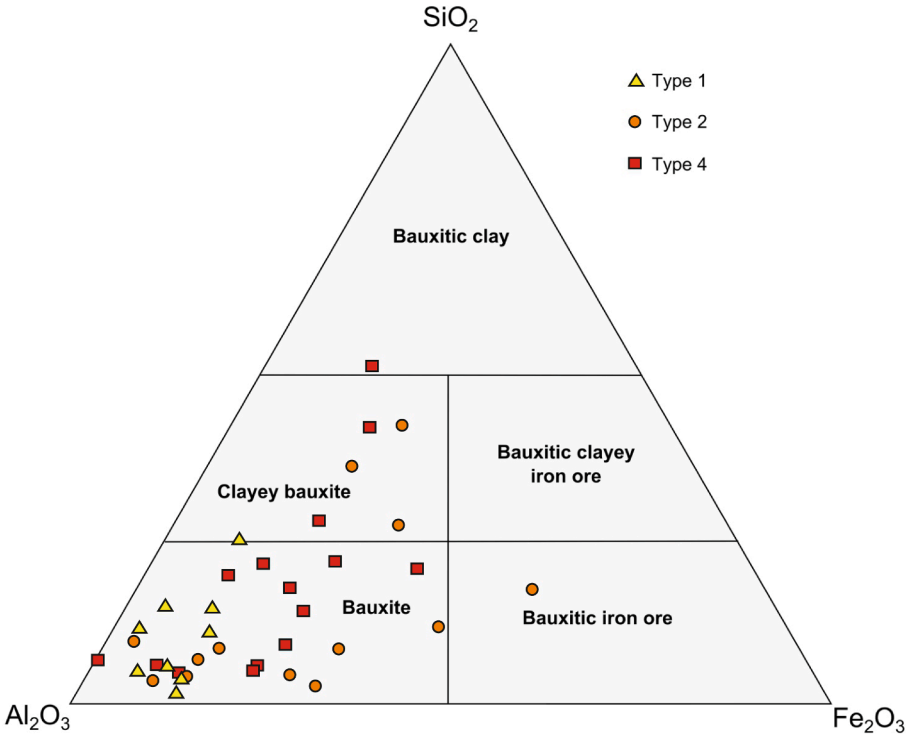

Fig. 5. SiO_2–Al_2O_3–Fe_2O_3 ternary diagram showing the classification of the Sardinian bauxite deposits.

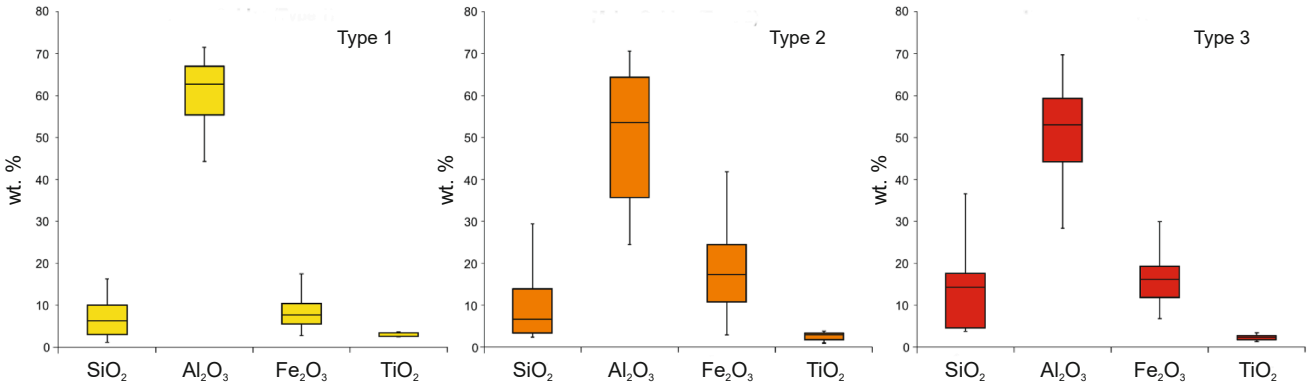

Fig. 6. Box-and-whisker plots showing the minimum, maximum, median, and first and third quartile values for major elements in the Sardinian bauxite deposits.

6. Discussion

6.1. *Factors affecting the distribution of critical metals in the Sardinian bauxites*

For the different bauxite types, Eu/Eu* values have been used to assess the provenance of karst bauxites (Abedini et al., 2020, and references therein). These values are similar to those of the Cretaceous alterite found below the bauxite and Messinian alterite derived from Variscan basement (average Eu/Eu* = 0.70 and 0.69, respectively), indicating the Sardinian bauxite types have the same provenance, as suggested by Mameli et al. (2007, 2020). This suggests that the differences in the compositions of the bauxite deposits are due to environmental differences during bauxitization of a common alluvial precursor. In order to elucidate the different environmental conditions, we evaluated the inter-elemental relationships between the major elements SiO_2, Al_2O_3, TiO_2, and Fe_2O_3, and the critical metals by R-mode factor analysis. The factors were extracted after Varimax rotation using the STATGRAPHICS 18 package. This operation was performed using a standardised correlation matrix, which is a classical type of factoring, thereby weighting all the variables equally during the factor calculations. The communalities provide an index of the efficiency of the proposed set of factors (Davis, 1986), and the magnitude of the communalities calculated in this study suggests that most of the original variance can be accounted for by the current set of factors.

Due to the different distributions of both LREEs and HREEs, type 4 deposits were considered separately from type 1 and 2 deposits. Type 1 and 2 deposits were merged into a single dataset.

6.1.1. *Inter-elemental relationships in the type 1 and 2 dataset*

Four factors explain 87.6% of the total variance in the type 1 and 2 dataset, including SiO_2, Al_2O_3, TiO_2, Fe_2O_3, LREEs, HREEs, Sc, V, Co, Ga, Sr, Nb, Hf, Ta, and W (Table 3). The first factor (F1; variance = 56.9%) includes significant and positive weightings for TiO_2, Nb, Hf, Ta, and W. Titanium, Nb, and Ta have similar geochemical properties and are often associated in karst bauxites (Mongelli et al., 2016, 2017;

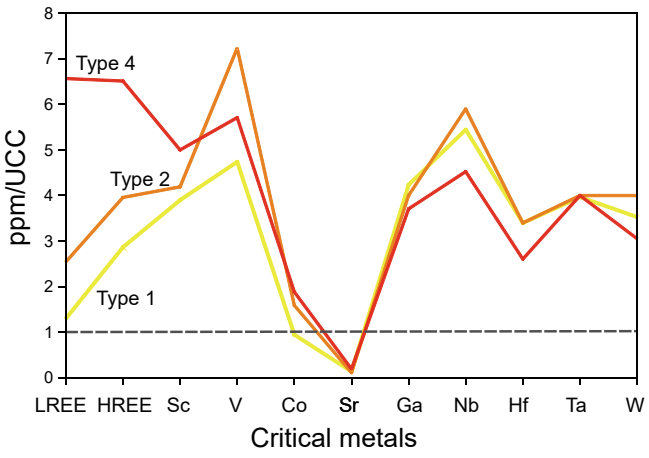

Fig. 7. Upper continental crust (UCC)-normalised diagram of CRM contents in the different bauxite types. UCC values are from McLennan et al. (2006).

Salamab-Ellahi et al., 2019; Abedini et al., 2020). Hafnium behaves similarly to Zr and the Hf–Zr correlation ($r = 0.99$) in this dataset is highly significant ($p < 0.01$). Tungsten typically occurs in low concentrations in natural waters, and is largely immobile (e.g., Bauer et al., 2018). Therefore, F1 represents the effect of low-solubility heavy minerals, including rutile, zircon, and scheelite, in controlling the Ti, Nb, Hf, Ta, and W contents in the type 1 and 2 dataset.

The second factor (F2) explains 14.6% of the total variance in the dataset. This factor includes significant and positive weightings for Al_2O_3, Sc, and Ga, and a significant negative weighting for SiO_2. The dominant silica-bearing mineral in both the type 1 and 2 bauxite deposits is kaolinite, which is confined to the matrix or micro-cracks as a secondary phase due to local re-silicification of boehmite. *In situ* boehmite epigenetic replacement of kaolinite during bauxitization can occur in a water-undersaturated environment that is characterised by a low water activity (Mongelli and Acquafredda, 1999; Mongelli, 2002). Gallium behaves similarly as Al, and bauxite can concentrate large amounts of this element (Schulte and Foley, 2013). Scandium is mined together with bauxite (Neikov et al., 2019). In the Parnassos–Ghiona bauxite deposit in Greece, Sc occurs mostly in hematite due to the Sc^{3+}–Fe^{3+} substitution (e.g., Gamaletsos et al., 2019), although there is a control exerted by Al oxyhydroxides, due to the Sc^{3+}–Al^{3+} substitution

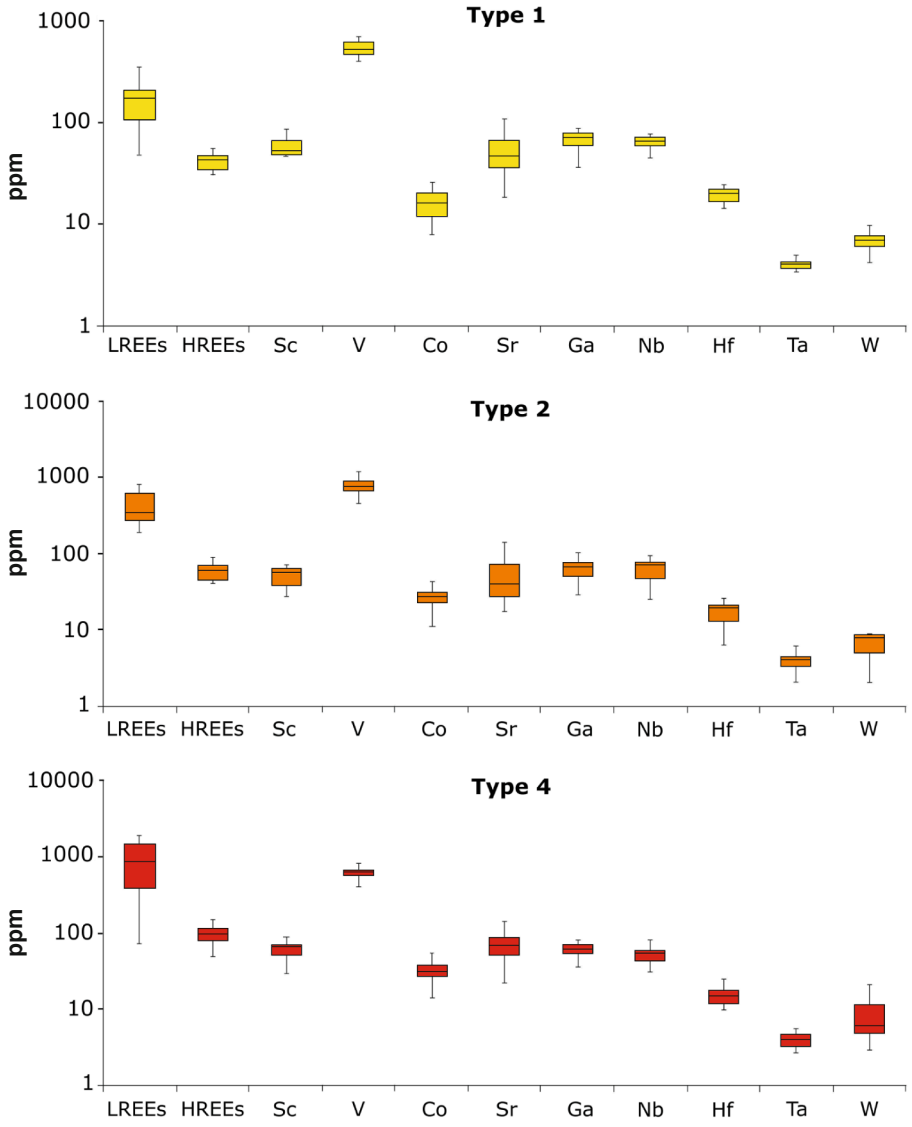

Fig. 8. Box-and-whisker plots showing the minimum, maximum, median, and first and third quartile values for the critical metals in the Sardinian bauxite deposits.

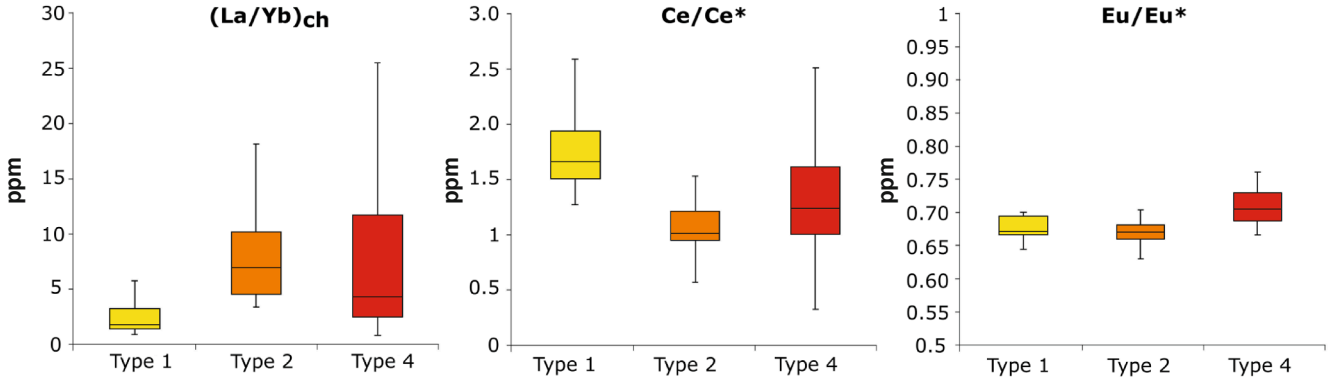

Fig. 9. Box-and-whisker plots showing the variation of minimum, maximum, median, and first and third quartile values for significant REE proxies ($(La/Yb)_{ch}$, Ce/Ce* and Eu/Eu*) in the Sardinian bauxite deposits studied.0

Table 3
Results of the R-mode factor analysis for both Type 1 + 2 and Type 4 deposits datasets. Numbers are weights of the variables in the extracted factors after Varimax rotation. Variables having weight<0.65 are omitted.

	Type 1 + 2 deposits				Type 4 deposit		
	F1	F2	F3	F4	F1	F2	F 3
SiO_2		−0.93			−0.75		
Al_2O_3		0.74			0.85		
Fe_2O_3				0.77			−0.78
TiO_2	0.86				0.86		
Sc		0.75				0.94	
V				0.76		0.88	
Co							−0.93
Ga		0.76			0.81		
Nb	0.88				0.86		
Hf	0.86				0.82		
Ta	0.87				0.79		
W	0.79				0.87		
LREE			0.75		−0.90		
HREE			0.87		−0.94		
Var. %	56.9	14.6	9.6	6.5	69.5	16.3	6.6

(Vind et al., 2018). In the Middle Timan bauxites in the Urals, Russia, Al oxyhydroxides are the primary source of Sc (Suss et al., 2017). Therefore, F2 represents the process related to drier conditions and the epigenetic replacement of kaolinite by boehmite, which likely incorporates Sc and Ga in its crystal structure.

The third factor (F3) explains 9.6% of the total variance in the dataset, and only the LREEs and HREEs have significant and positive weightings. REEs and particularly the LREEs are enriched in the illuvial horizon close to the carbonate bedrock, and occur mainly in cerianite and fluorocarbonates. The formation of cerianite occurs in karst bauxites (e.g., Mongelli et al., 1997, 2014), and requires Ce^{3+} oxidation to Ce^{4+} and subsequent CeO_2 precipitation in a pH range of 5–6, assuming a Ce activity of 10^{-9} M for Eh = 0.38–0.61 V, via the reaction (1):

$$Ce^{3+}_{(aq)} + 2H_2O = CeO_{2(s)} + 4H^+ + e^- \quad (1)$$

The occurrence of fluorocarbonates requires mobilisation of trivalent REEs (Ln = lanthanides) and fluoride complexation with further precipitation of the mineral near the carbonate bedrock barrier under alkaline pH conditions, via the reaction (2) (Mongelli, 1997):

$$2LnF^{2+}_{(aq)} + Ca^{2+}_{(aq)} + 3HCO_3^-{}_{(aq)} = Ln_2Ca(CO_3)_3F_{2(s)} + 3H^+_{(aq)} \quad (2)$$

As such, F3 accounts for the processes occurring mostly close to the bedrock in the illuvial horizon, which promoted REE mobilisation, oxidation, complexation, and further precipitation.

The fourth factor (F4) explains 6.5% of the total variance in the dataset, and this factor only has a significant positive weighting for Fe_2O_3 and V. Iron oxyhydroxides in karst bauxites are retained during wet conditions (e.g., Mongelli, 2002; Mameli et al., 2007; Mongelli et al., 2015; Yuste et al., 2020). Vanadium is also a redox-sensitive element, which occurs as V^{3+}, V^{4+}, and V^{5+}. Under most environmental conditions, V occurs mainly as the vanadate oxyanion (V^{5+}), which is strongly adsorbed as the bidentate complex onto Fe oxyhydroxides (Gustafsson, 2019). Thus, F4 accounts for the process promoting the formation of Fe oxyhydroxides, which controlled V through vanadate oxyanion adsorption under wetter conditions than those favouring boehmite replacement of kaolinite.

6.1.2. *Inter-elemental relationships in the type 4 dataset*

Three factors explain 92.4% of the total variance in the type 4 dataset, including SiO_2, Al_2O_3, TiO_2, Fe_2O_3, LREEs, HREEs, Sc, V, Co, Ga, Nb, Hf, Ta, and W (Table 3). Given that the selected variables used to perform the R-mode factor analysis have to be n–1, where n is the number of samples, we arbitrarily decided to exclude Sr from the variables.

The first factor (F1; variance = 69.5%) includes significant and positive weightings for Al_2O_3, TiO_2, Ga, Nb, Hf, Ta, and W, and significant negative weightings for SiO_2, LREEs, and HREEs. Aluminium and Ti accumulate during bauxitization and most of the critical metals with positive weightings exhibit similar geochemical behaviour as Al (Ga) and Ti (Nb and Ta), or can be hosted in detrital minerals including zircon (Hf–Zr correlation; r = 0.98) and W-rich phases. Furthermore, as also observed in the type 1 and 2 dataset, the negative weighting of SiO_2 is likely related to the epigenetic replacement of kaolinite by boehmite. Authigenic REE-bearing fluorocarbonates occur in the type 4 bauxite deposits, especially in the illuvial horizons where ΣREEs = 1006–2034 ppm (Ce = 374–1280 ppm), and are concentrated in the aphanitic silica-rich matrix. F1 is similar to F2 for the type 1 and 2 dataset, and likely represents silica depletion under drier conditions, which allowed the formation and stability of a range of minerals including Al and Ti oxyhydroxides and detrital minerals.

The second factor (F2) explains 16.3% of the total variance in the dataset. This factor includes significant and positive weightings for Sc and V. Scandium is different to V and is not a redox-sensitive element, and occurs mainly as Sc^{3+}. In karst bauxites and laterites, Sc usually covaries with Fe and generally occurs in Fe oxyhydroxides or as an adsorbed or substituted ion for Fe^{3+} in hematite (Chassé et al., 2017; Vind et al., 2018). In karst bauxites, this mechanism has been suggested to explain the V^{3+} covariance with Fe^{3+} (Khosravi et al., 2017; Mongelli et al., 2017). V^{3+} exists in reducing conditions (Gustafsson, 2019) and the significant V–U correlation ($r = 0.66$; $p < 0.01$) suggests these conditions existed during the bauxitization of the type 4 deposits. Furthermore, the absence of a correlation between both Sc and V with

Fe, as well as their ability to substitute for other ions in mineral structures (Vind et al., 2018; Gustafsson, 2019), indicate Sc and V were probably controlled by a range of minerals and not solely by Fe phases.

The third factor (F3) has significant and positive weightings for Fe_2O_3 and Co. Fe_2O_3–Co correlations are a common feature of several Cretaceous Tethyan karst bauxite deposits (Mongelli et al., 2017). During intense weathering, Co^{2+} is soluble in the metal–O–H system under mildly alkaline to acidic conditions throughout a wide Eh range (Gaillardet et al., 2003). The maximum Co^{2+} uptake by hematite occurs under alkaline conditions (Su, 2011) as ferric hydroxides at low pH have mainly protonated sites, with the surface maintaining a net positive charge that gradually decreases as pH increases. This reduces the electrical repulsion between the adsorbing surface and cations (Lee and Saunders, 2003). Therefore, F3 represents the capability of Fe oxyhydroxides to control Co through adsorption.

6.2. *Supply risk and economic importance: Clues for potential profitability*

Intense weathering of peralkaline or carbonatitic rocks can generate bauxite and laterite ores with a high grade of REEs and other CRM (Witt et al., 2019). China is the main producer of REEs due to its numerous carbonatite-related REE ores (Xu et al., 2008; Xie et al., 2015; Ni et al., 2020). Outside China, the main economic REE deposits are hydrothermal and metasomatic (i.e., fenitic) ores associated with alkaline and peralkaline magmas (Goodenough et al., 2016; Goodenough et al., 2018). Mafic igneous rocks are not associated with REE ores (Das et al., 2020), and karstic bauxite formed on sediments from mafic rocks also do not form REE deposits (e.g., Liu et al., 2010; Abedini et al., 2021).

In general, intense weathering of metamorphic and granitic rocks forms bauxite and laterite with a wide range of REE and other CRM contents, which is also the case for the Sardinian bauxites. The studied bauxites have higher median LREE, HREE, Sc, and V contents in the type 4 deposits, and V, Ga, Nb, Hf, and W contents in the type 1 and 2 deposits, as compared with other Mediterranean-type bauxites (Fig. 10). It is worth noting that, in our knowledge, a REEs content magnitude similar to that detected in type 4 is observed in a few levels of Chinese karst bauxites derived from a cratonic precursor (Li et al., 2013; Yang et al., 2019; Liu et al., 2020). Further, within the European economic scenario, the total rare earth oxide (TREO) content of 0.18 wt% of the illuvial horizon in the type 4 bauxite deposits compares favourably with the TREO cut-off of the Norra Karr mine in Sweden (0.2 wt%; GBM project 0465, 2015), suggesting this type of Sardinian bauxite could be a future REE source. Whether an element is of economic interest or not depends on the criticality of the metal. In the EU, the assessment of criticality depends on risk supply and economic importance (European Commission, 2017). In general, a low ratio of the economic importance (EI) to supply risk (SR) (European Commission, 2020), as is the case for LREEs and HREEs (EI/SR < 1), suggests a supply risk, whereas a larger ratio (EI/SR > 2) indicate significant economic importance, as is the case for Co, V, Ga, Ta, Hf, and W.

For the Sardinian bauxite deposits, the EI/SR ratio and range of CRM contents normalised to the average UCC (Fig. 11), indicate that the type 4 deposits host CRM characterised by supply risk, such as the LREEs and HREEs, and also economic importance (EI/SR > 5), such as W. Type 1 and 2 deposits preferentially concentrate V (EI/SR $= 2.6$) and, to a lesser extent, Ga (EI/SR $= 2.75$) and Ta (EI/SR $= 2.87$) as compared with the type 4 deposits.

7. Summary and conclusions

In the Sardinian bauxite deposits, boehmite is the main Al-phase, whereas diaspore and gibbsite only occur occasionally or are negligible in content. Kaolinite is the main silica-rich mineral, and hematite and goethite are the only Fe phases. Secondary anatase and detrital rutile host Ti. Residual detrital minerals, such as rutile, scheelite, zircon,

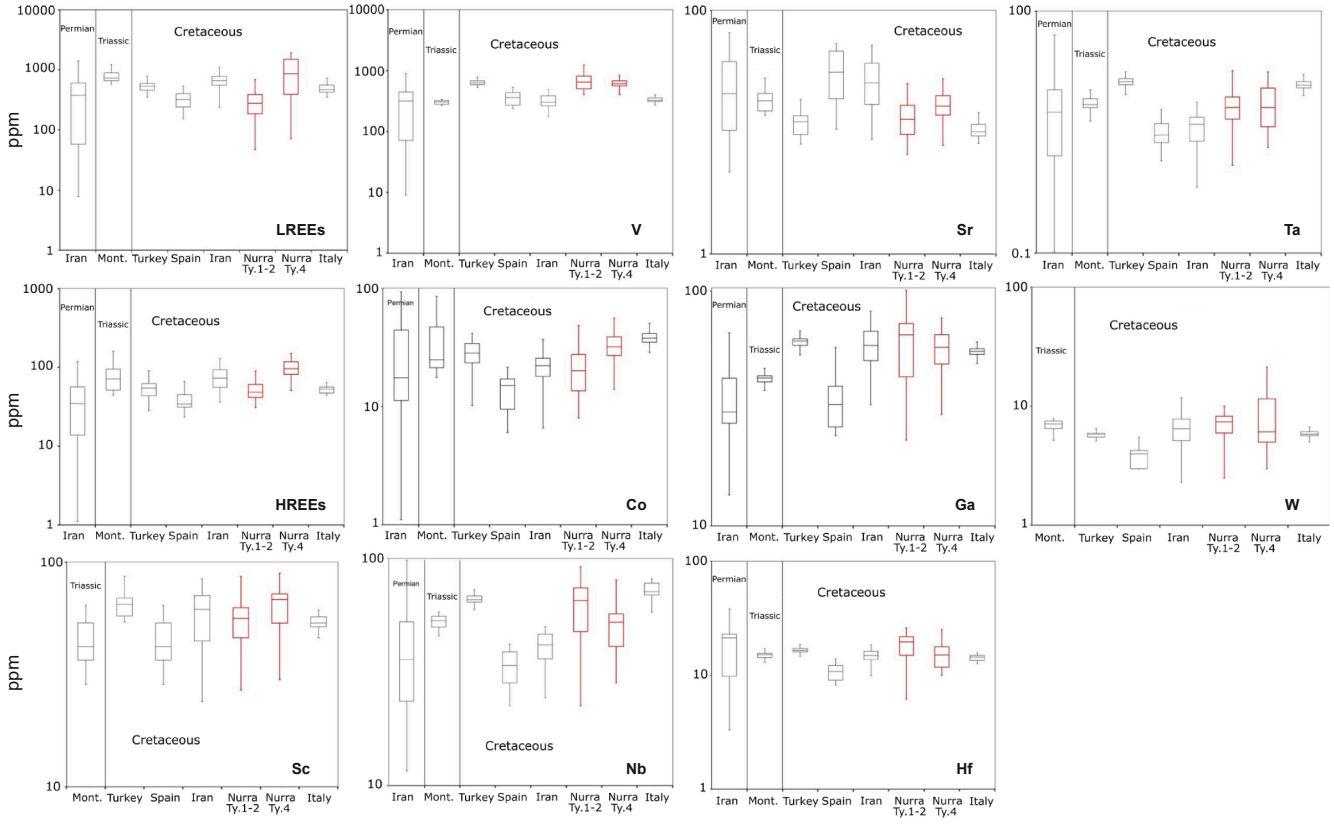

Fig. 10. Box-and-whisker plots showing the variation of critical metal contents in different Mediterranean-type bauxite ores.

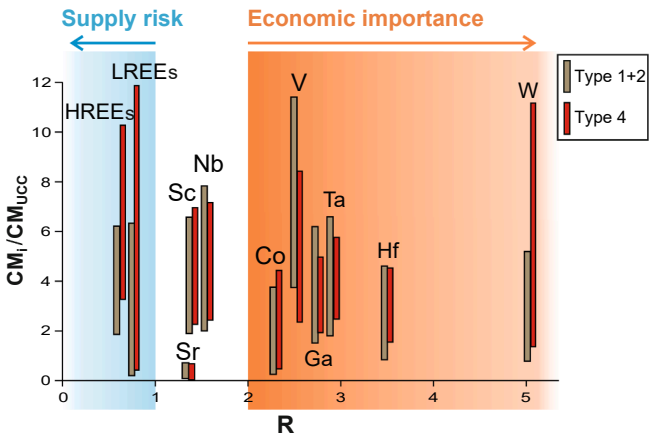

Fig. 11. CRM profitability diagram for the Sardinian bauxite ores. R = economic importance/supply risk; CM_i/CM_{UCC} = minimum–maximum range of critical metal normalised to its average UCC content.

and monazite, are generally distributed throughout the whole bauxite deposit profiles. Neoformed REE-bearing fluorocarbonates are confined to the illuvial horizon as intergrowths with boehmite and/or Fe oxy-hydroxides, which is suggestive of a diagenetic origin. In contrast, cerianite occurs in association with post-diagenetic Fe hydroxides in veins or within oxidised marcasite and pyrite.

Eu/Eu* values clearly show that the Sardinian bauxite types have the same provenance, although there are differences in Al_2O_3 and SiO_2 contents. The differences between the silica-poor type 1 and 2 and silica-rich type 4 deposits suggest the former was formed in a drier climate, which promoted pervasive epigenetic replacement of kaolinite by boehmite.

R-mode factor analysis suggests that most CRM, such as Sc and Ga in the type 1 and 2 dataset, and Ga, Nb, Hf, Ta, and W in the type 4 dataset, covary with Al_2O_3. In the type 1 and 2 deposits, Sc and Ga are likely hosted in the boehmite crystal structure, whereas in the type 4 deposits, CRM are mostly hosted by residual detrital minerals. Fe_2O_3 may control V and Co contents via adsorption mechanisms.

SEM-EDS observations indicate that REE-rich minerals, including fluorocarbonates and cerianite, are concentrated in the illuvial horizon, especially in the type 4 deposits where ΣREE = 1006–2034 ppm. Cerianite formation requires Ce oxidation, whereas fluorocarbonate formation involves mobilisation of trivalent REEs and fluoride complexation. Both minerals were precipitated under alkaline pH conditions close to the carbonate bedrock.

The evaluation of the CRM in the Sardinian bauxites coupled with the economic importance and supply risk indicate these deposits contain large amounts of CRM characterised by a supply risk, such as the LREEs and HREEs, and economic importance, such as V and W. These new data, in the light of the growing European high-tech industry demand of CRM, especially REEs, may be helpful for stakeholders suggesting that the Sardinian bauxite, at the present unexploited, may deserve a new profitable chance of exploitation.

Declaration of Competing Interest

The authors declare that they have no known competing financial interests or personal relationships that could have appeared to influence the work reported in this paper.

Acknowledgments

The authors are grateful to the three anonymous reviewers and the Associate Editor (Prof. Ibrahim Uysal) for the useful suggestions and the improvement of the manuscript and to Dr. Giovanni L. Cardello (University of Sassari) for redrawing the geological sketch map.

This work was financially supported by the University of Sassari (Fondo di Ateneo per la Ricerca 2020 – Paola Mameli) and a Prof. Giovanni Mongelli grant (RIL 2019, Italy).

References

Abedini, A., Mongelli, G., Khosravi, M., 2021. Geochemical constraints on the middle Triassic Kani Zarrineh karst bauxite deposit, Irano-Himalayan belt, NW Iran: Implications for elemental fractionation and parental affinity. Ore Geol. Rev. 133, 104099. https://doi.org/10.1016/j.oregeorev.2021.104099.

Abedini, A., Mongelli, G., Khosravi, M., Sinisi, R., 2020. Geochemistry and secular trends in the middle–late Permian karst bauxite deposits, northwestern Iran. Ore Geol. Rev. 124, 103660. https://doi.org/10.1016/j.oregeorev.2020.103660.

Bardossy, G., 1982. Karst Bauxites, bauxite deposits on carbonate rocks. In: Developments in Economic Geology, volume 14. Elsevier Scientific, Amsterdam, pp. 1–441.

Bardossy, G., Aleva, G.J.J., 1990. Lateritic Bauxites. In: Developments in Economic Geology, volume 27. Elsevier Scientific, Amsterdam, pp. 1–624.

Bauer, S., Conrad, S., Ingri, J., 2018. Geochemistry of tungsten and molybdenum during freshwater transport and estuarine mixing. App. Geochem. 93, 36–48. https://doi.org/10.1016/j.apgeochem.2018.03.015.

Blanc, J.J., Gouvernet, C., 1967. L'isthme durancien en Basse-Provence occidentale. Bull. Soc. Géol. de France S7-IX (4), 631–639. https://doi.org/10.2113/gssgfbull.S7-IX.4.631.

Bogatyrev, B.A., Zhukov, V.V., 2009. Bauxite provinces of the world. Geol. Ore Depos. 51 (5), 339–355. https://doi.org/10.1134/S1075701509050018.

Chakhmouradian, A.R., Smith, M.P., Kynickly, J., 2015. From "strategic" tungsten to "green" neodymium: a century of critical metals at a glance. Ore Geol. Rev. 64, 455–458. https://doi.org/10.1016/j.oregeorev.2014.06.008.

Chassé, M., Griffin, W.L., O'Reilly, S.Y., Calas, G., 2017. Scandium speciation in a world-class lateritic deposit. Geochem. Perspect. Lett. 3, 105–114. https://doi.org/10.7185/geochemlet.1711.

Combes P.J., Oggiano G., Temussi I., 1993. Geodynamique des bauxites sardes, typologie, génese controle paleotectonique. Comptes Rendus de l'Académie des Sciences Sèrie II 316, 403-409.

Das, B., Khan, M.W.Y., Dhruw, H., 2020. Trace and REE geochemistry of bauxite deposit of Darai-Daldali plateau, Kabirdham district, Chhattisgarh. India. J. Earth Syst. Sci. 129, 117. https://doi.org/10.1007/s12040-020-1377-1.

Davis, J.C., 1986. Statistics and Data Analysis in Geology. John Wiley & Sons, New York.

Commission, E., 2017. Methodology for establishing the EU list of critical raw materials. Guidelines, Directorate-General for Internal Market, Industry, Entrepreneurship and SMEs, p. 30.

European Commission, 2020. Study on the EU's list of Critical Raw Materials Critical Raw Materials, Factsheets (Final). Directorate-General for Internal Market, Industry, Entrepreneurship and SMEs, Joint Research Centre Directorate GROW.C, JRC.D Unit GROW.C.2 Energy-intensive Industries and Raw Materials, JRC.D.3 Land Resources, 819 pp.

Gaillardet J., Viers J., Dupre B., 2003. Trace elements in river waters, in: Drever, J.I. (Ed.), Treatise on Geochemistry. Elsevier-Pergamon, Oxford, pp. 225-272. https://doi.org/10.1016/B0-08-043751-6.

Gamaletsos, P.N., Godelitsas, A., Filippidis, A., Pontikes, Y., 2019. The Rare Earth Elements potential of greek bauxite active mines in light of a sustainable REE demand. J. Sust. Metallur. 5, 20–47. https://doi.org/10.1007/s40831-018-0192-2.

GBM, 2015. Amended & restated prefeasibility study – NI 43-101 – technical report for the Norra Kärr Rare Earth Element deposit – prepared for Tasman Metals Ltd. GBM Project Number: 0465. Gränna, Sweden, pp. 376.

Goodenough, K.M., Schilling, J., Jonsson, E., Kalvig, P., Charles, N., Tuduri, J., Deady, E. A., Sadeghi, M., Schiellerup, H., Müller, A., Bertrand, G., Arvanitidis, N., Eliopoulos, D.G., Shaw, R.A., Thrane, K., Keulen, N., 2016. Europe's rare earth element resource potential: an overview of REE metallogenetic provinces and their geodynamic setting. Ore Geol. Rev. 72, 838–856. https://doi.org/10.1016/j.oregeorev.2015.09.019.

Goodenough, K.M., Wall, F., Merriman, D., 2018. The rare earth elements: demand, global resources, and challenges for resourcing future generations. Nat. Resour. Res. 27 (2), 201–216. https://doi.org/10.1007/s11053-017-9336-5.

Graedel, T.E., Harper, E.M., Nassar, N.T., Nuss, P., Reck, B.K., 2015. Criticality of metals and metalloids. PNAS 112 (14), 4257–4262. https://doi.org/10.1073/pnas.1500415112.

Gunn G., 2014. Critical Metals Handbook, first ed. John Wiley & Sons, Ltd. https://doi.org/10.1002/9781118755341.

Gustafsson, J.P., 2019. Vanadium geochemistry in the biogeosphere –speciation, solid-solution interactions, and ecotoxicity. App. Geochem. 102, 1–25. https://doi.org/10.1016/j.apgeochem.2018.12.027.

Guyonnet, D., Planchon, M., Rollat, A., Escalon, V., Tuduri, J., Charles, N., Vaxelaire, S., Dubois, D., Fargier, H., 2015. Material flow analysis appliedto rare earth elements in Europe. J. Clean. Prod. 107, 215–228. https://doi.org/10.1016/j.jclepro.2015.04.123.

Jaroni, M., Friedrich, B., Letmathe, P., 2017. Criticality of Rare Earth Metals: a European analysis. Working Paper. RWTH Aachen University, Aachen, Germany.

Khosravi, M., Abedini, A., Alipour, S., Mongelli, G., 2017. The Darzi-Vali bauxite deposit, West-Azarbaidjan Province, Iran: critical metals distribution and parental affinities. J. Afr. Earth Sci. 129, 960–972. https://doi.org/10.1016/j.jafrearsci.2017.02.024.

Lee, M., Saunders, J.A., 2003. Effects of pH on metals precipitation and sorption: field bioremediation and geochemical modelling approaches. VZJ 2, 177–185. https://doi.org/10.2113/2.2.17.

Li, Z., Din, J., Xu, J., Liao, C., Yin, F., Lu, T., Cheng, L., Li, J., 2013. Discovery of the REE minerals in the Wulong-Nanchuan bauxite deposits, Chongqiong, China: insights on conditions of formation and processes. J. Geochem. Expl. 133, 88–102. https://doi.org/10.1016/j.gexplo.2013.06.016.

Liu, X., Wang, Q., Deng, J., Zhang, Q., Sun, S., Meng, J., 2010. Mineralogical and geochemical investigations of the Dajia Salento-type bauxite deposits, western Guangxi. China. J. Geochem. Expl. 105 (3), 137–152. https://doi.org/10.1016/j.gexplo.2010.04.012.

Liu, X., Wang, Q., Zhao, L., Peng, Y., Ma, Y., Zhou, Z., 2020. Metallogeny of the large-scale Carboniferous karstic bauxite in the Sanmenxia area, southern part of the North China Craton, China. Chem. Geol. 556, 119851. https://doi.org/10.1016/j.chemgeo.2020.119851.

MacLean, W.H., Bonavia, F.F., Sanna, G., 1997. Argillite debris converted to bauxite during karst weathering: evidence from immobile element geochemistry at the Olmedo Deposit, Sardinia. Miner. Depos. 32 (6), 607–616. https://doi.org/10.1007/s001260050126.

Mameli, P., Mongelli, G., Oggiano, G., Dinelli, E., 2007. Geological, geochemical and mineralogical features of some bauxite deposits from Nurra (Western Sardinia, Italy): insights on conditions of formation and parental affinity. Int. J. Earth Sci. 96 (5), 887–902. https://doi.org/10.1007/s00531-006-0142-2.

Mameli, P., Mongelli, G., Sinisi, R., Oggiano, G., 2020. Weathering products of a dismantled Variscan basement. Minero-chemical proxies to insight on Cretaceous palaeogeography and Late Neogene palaeoclimate of Sardinia (Italy). Front. Earth Sci. 290 (8), 1–20. https://doi.org/10.3389/feart.2020.00290.

McLennan, S.M., Taylor, S.R., Hemming, S.R., 2006. Composition, differentiation and evolution of continental crust: constrains from sedimentary rocks and heat flow. In: Brown, M., Rushmer, T. (Eds.), Evolution and Differentiation of The Continental Crust. Cambridge University Press, Cambridge, pp. 92–134.

Mongelli, G., 1997. Ce-anomalies in the textural components of Upper Cretaceous karst bauxites from the Apulian carbonate platform (southern Italy). Chem. Geol. 140 (1-2), 69–79. https://doi.org/10.1016/S0009-2541(97)00042-9.

Mongelli, G., 2002. Growth of hematite and boehmite in concretions from ancient karst bauxite: clue for past climate. Catena 50 (1), 43–51. https://doi.org/10.1016/S0341-8162(02)00067-X.

Mongelli, G., Acquafredda, P., 1999. Ferruginous concretions in a Late Cretaceous karst bauxite: composition and conditions of formation. Chem. Geol. 158 (3-4), 315–320. https://doi.org/10.1016/S0009-2541(99)00061-3.

Mongelli, G., Boni, M., Buccione, R., Sinisi, R., 2014. Geochemistry of the Apulian karst bauxites (Southern Italy): chemical fractionation and parental affinities. Ore Geol. Rev. 63, 9–21. https://doi.org/10.1016/j.oregeorev.2014.04.012.

Mongelli, G., Boni, M., Oggiano, G., Mameli, P., Sinisi, R., Buccione, R., Mondillo, N., 2017. Critical metals distribution in Tethyan karst bauxite: the Cretaceous Italian ores. Ore Geol. Rev. 86, 526–536. https://doi.org/10.1016/j.oregeorev.2017.03.017.

Mongelli, G., Buccione, R., Gueguen, R., Langone, A., Sinisi, R., 2016. Geochemistry of the Apulian allochthonous karst bauxite, Southern Italy: Distribution of critical elements and constraints on Late Cretaceous Peri-Tethyan palaeogeography. Ore Geol. Rev. 77, 246–259. https://doi.org/10.1016/j.oregeorev.2016.03.002.

Mongelli, G., Buccione, R., Sinisi, R., 2015. Genesis of autochthonous and allochthonous Apulian karst bauxites (Southern Italy): climate constraints. Sediment. Geol. 325, 168–176. https://doi.org/10.1016/j.sedgeo.2015.06.005.

Neikov, O.D., Naboychenko, S.S., Murashova, I.B., 2019. Production of rare metal powders. In: Neikov, O.D., Naboychenko, S.S., Yefimov, N.A. (Eds.), Handbook of Non-Ferrous Metal Powders (Second Edition). Elsevier, USA, pp. 757–829. https://doi.org/10.1016/B978-0-08-100543-9.00024-5.

Ni, P., Zhou, J., Chi, Z., Pan, J.-Y., Li, S.-N., Ding, J.-Y., Han, L., 2020. Carbonatite dyke and related REE mineralizationin the Bayan Obo REE ore field, North China: Evidence from geochemistry, C-O isotopes and Rb-Sr dating. J. Geochem. Explor. 215, 106560. https://doi.org/10.1016/j.gexplo.2020.106560.

Salamab-Ellahi, S., Taghipour, B., Mongelli, G., 2019. Clayey bauxite from the Irano-Himalayan belt: critical metals, provenance and palaeoclimate in the Upper Cretaceous Semirom ore deposit, Zagros Mountain. Iran. J. Asian Earth Sci. 172, 126–142. https://doi.org/10.1016/j.jseaes.2018.09.001.

Schreiber, D., Giannerini, G., Lardeaux, J.M., 2011. The Southeast France basin during Late Cretaceous times: The spatiotemporal link between Pyrenean collision and Alpine subduction. Geodin. Acta 24, 21–35. https://doi.org/10.3166/ga.24.23-37.

Schulte R.F., Foley N.K., 2013. Compilation of Gallium resource data for Bauxite deposits, U.S. Department of the Interior, U.S. Geological Survey, Open-File Report 2013-1272, 14 pp. https://dx.doi.org/10.3133/ofr20131272.

Su, L.W., 2011. Cobalt Adsorption and/or Co-Precipitation Onto Ferric Oxyhydroxide. The University of British Columbia, Vancouver, p. 94.

Suss, A., Kuznetsova, N.V., Kozyrev, A., Panov, A., Gorbachev, S., 2017. Specific features of scandium behavior during sodium bicarbonate digestion of red mud, in: Proceedings, Travaux 46. In: Presented at the 35th International ICSOBA Conference, pp. 491–504.

Vind J., Malfliet A., Bonomi C., Paiste P., Sajo I.E., Blanpain B., Tkaczyk A.H., Vassiliadou V., Panias D., 2018. Modes of occurrences of scandium in Greek bauxite and bauxite residue. Miner. Eng. 123, 35-48. https://doi.org/ 10.1016/j.mineng.2018.04.025.

Witt, W.K., Hammond, D.P., Hughes, M., 2019. Geology of the Ngualla carbonatite complex, Tanzania, and origin of the Weathered Bastnaesite Zone REE ore. Ore Geol. Rev. 105, 28–54. https://doi.org/10.1016/j.oregeorev.2018.12.002.

Xie, Y., Li, Y., Hou, Z., Cooke, D.R., Danyushevsky, L., Dominy, S.C., Yin, S., 2015. A model for carbonatite hosted REE mineralisation — the Mianning–Dechang REE belt, Western Sichuan Province. China. Ore Geol. Rev. 70, 595–612. https://doi.org/10.1016/j.oregeorev.2014.10.027.

Xu, C., Campbell, I.H., Kynicky, J., Allen, C.M., Chen, Y., Huang, Z., Qi, L., 2008. Comparison of the Daluxiang and Maoniuping carbonatitic REE deposits with Bayan Obo REE deposit, China. Lithos 106 (1-2), 12–24. https://doi.org/10.1016/j.lithos.2008.06.005.

Yang, S.J., Huang, Y.X., Wang, Q.F., Deng, J., Liu, X.F., Wang, J.Q., 2019. Mineralogical and geochemical features of karst bauxites from Poci (western Henan, China), implications for parental affinity and bauxitization. Ore Geol. Rev. 105, 295–309. https://doi.org/10.1016/j.oregeorev.2018.12.028.

Yuste, A., Camacho, I., Bauluz, B., Mayayo, M.J., Laita, E., 2020. Palaeoweathering events recorded on siliciclastic continental deposits (Albian, Lower Cretaceous) in NE Spain. Appl. Clay Sci. 190, 105598. https://doi.org/10.1016/j.clay.2020.105598.